Polyethylene-based Microfluidic System Approaches to Achieve Adaptive Visible and Thermal Camouflage Applications

by

Xiaoruo Sun

A thesis submitted in partial fulfillment of the requirements for the degree of

Master of Science

Department of Mechanical Engineering

University of Alberta

Abstract

Camouflage represents a critical skill in both nature and combat zones, as it enables concealment from potential threats. With the advancement of visual and infrared-sensitive surveillance equipment, adaptive camouflage across the visible and infrared (IR) spectrums has become increasingly important due to the advantage of blend in the background. Therefore, the low-cost, high-speed fabrication of adaptive visible and infrared camouflage control system has gained significant attention. Microfluidic devices have a high potential for achieving adaptive multiband camouflage including both visible and infrared (IR) spectrums because they can manipulate fluids that may be dyed, transparent, or opaque to different parts of the electromagnetic spectrum. In the initial phase of this thesis work, we developed a high-speed, low-cost robust process to fabricate microfluidic devices entirely made from polyethylene using xurography and thermocompression molding techniques. Moreover, a novel method that thermally bond macro-scale polyethylene tubing to micro-scale channels is developed. The simplicity and flexibility of the method allow the fabrication of devices with different channel heights, widths, and patterns. Upon filling the microfluidic devices with dyed liquids and testing them with different backgrounds, the devices showed fast and high adaptive visible camouflage capabilities. Moreover, the thermal IR appearance of microfluidic systems can be altered without changing temperature by incorporating a metalized surface which can be covered by an IR opaque liquid to alter the apparent temperature when reflecting IR sources. However, the long actuation times and unfavorable scaling laws for pressure-driven flows in smaller channels posed challenges for rapid fluid actuation. To address this, the second phase of this work focused on replacing the pressure-driven flow with an electrowetting system, capable of fast-actuating droplets using low voltage while preserve the capabilities to achieve adaptive infrared camouflage. We developed and conducted an initial feasibility test for an electrowetting on dielectric (EWOD) system based on simple fabrication techniques without atomic deposition for adaptive infrared camouflage. The electrowetting of a drop of water within an IR transparent oil (dodecane) can occur between an aluminum electrode surface with a self-assembled lipid bilayer as the dielectric. This lipid dielectric bilayer both reduces required electrowetting voltage to below 5V and is spontaneously formed in the system. More importantly, the thermal appearance of the electrodes can be altered upon wetting the droplet when reflecting IR sources with a fast actuation time (about one second). The thickness of the dodecane must be less than 1 mm before it is sufficiently transparent for thermal IR to function effectively as an IR variable pixel, but this technique may hold promise to produce faster switching and more effective microfluidic-based thermal camouflage in the future.

Keywords: *Microfluidic devices, Adaptive visible camouflage, Adaptive Infrared camouflage, Polyethylene, UHMWPE, Flexible microfluidic devices, Macro-to-Micro interface, Infrared Characterization, Infrared reflectance, Infrared absorbance, Boundary detection, Electrowetting (Digital Microfluidic), Lipid Bilayer*

Preface

This master dissertation is an original work by Xiaoruo Sun. Chapter 2 is published in Advanced Material Technologies. Chapter 3 is under preparation for submission.

1. Xiaoruo Sun, et al. “Low-Cost and High-Speed Fabrication of Camouflage-Enabling Microfluidic Devices using Ultrahigh Molecular Weight Polyethylene.” *Advanced Materials Technologies* (2023), 2300705
2. Xiaoruo Sun, et al. “Low voltage actuated complete electrowetting phenomenon on metalized polyester.” Under preparation for submission as a journal article

Dedicated to my loving parents,

Yunyu Hou, Gang Sun

For their endless love, understanding, and unwavering support through all times.

Acknowledgement

I would like to express my deepest gratitude to my supervisor, Dr. Sameoto, for his continuous support, guidance, and mentorship throughout the entire journey of this thesis. Without his encouragement and patience, this research would not have been possible. I cannot adequately express my respect and thankfulness to you. You trusted me to join your group as the very first master's student during the pandemic and have always been there for me through the hard times. It really means a lot to me to be your student. Thank you for everything!

I would like to thank my thesis examiner Prof. Anastasia Elias and Prof. James Hogan for their support.

Special thanks to the post-doctoral fellowship colleague in our group Dr. Asad for his endless support and guidance.

Special thanks to my colleagues: Mehnab Ali, Luka Morita, Zhaoqi Ma, Abolfazl Vaheb, Shima Jalali for all the happy memories we have had together.

This research is funded by: Department of National Defence (DND) of Canada program Innovation for Defence Excellence and Security (IDEaS) and Natural Sciences and Engineering Research Council of Canada (NSERC) Alliance – Alberta Innovates (AI) Advance Program.

Table of Contents

List of Tables

Table of Figures

Chapter 1

Introduction

1.1 Research Objectives

This work aims to design, investigate, test, and characterize innovative adaptive multi-spectrum camouflage control methods through the use of microfluidic/digital microfluidic devices. Several key features are emphasized, including cost-effectiveness, energy efficiency, short fabrication time, simplicity in fabrication, robustness, reusability, and reconfigurability. For these purposes, the research work has been divided into two paper-based chapters:

- In Chapter 2, a microfluidic device is designed and characterized to achieve multi-spectrum camouflage control within a thermally and visibly semi-transparent polymer (Ultra-high molecular weight polyethylene, UHMWPE). Considering the key features of interest, the device fabrication process does not include micro-fabrication and etching, and a clean-room condition is not required. Owing to the nature of UHMWPE, it develops a high-speed, low-cost robust process to fabricate microfluidic devices using xurography and thermocompression molding techniques. Moreover, a novel method that thermally bond macro-scale polyethylene tubing to micro-scale device channels is developed. The camouflage performance is extensively characterized through. Scanning Electron Microscopic (SEM) observation, FTIR and UV-Vis analysis, visual background matching analysis, average RGB colour matching analysis, colour pattern matching analysis, infrared reflectance appearance testing, and computerized edge detection analysis.
- In Chapter 3, an electrowetting device is designed and characterized to determine its feasibility for IR variable camouflage. Electrowetting, which is also known as digital microfluidics, shares similar functionality as the device developed in Chapter 2. The regular microfluidic device uses pressure-driven flow, whereas the electrowetting device utilizes a low voltage-actuated droplet. The electrowetting device does not require any

atomic or thin film depositions. Multiple modifications are applied to the device with all design choices being made toward IR camouflage. The configuration includes planar electrodes and very thin layer of dodecane which improves the IR appearance. The device is characterized through digital tensiometer observations, infrared reflectance appearance testing, capacitance measurements, and infrared absorbance analysis.

1.2 Thesis Structure

This is a paper-based master dissertation that contains four chapters. Chapter 2 is published, while Chapter 3 is under preparation for submission.

Chapter 1 provides detailed background information about several major topics to offer a more comprehensive understanding of this thesis work. It presents a brief overview of microfluidic devices, including their classification based on fabrication techniques, applications, and materials used. The chapter also introduces the concept of the Macro-to-Micro interface in microfluidic devices. There's an in-depth look at polyethylene, specifically distinguishing UHMWPE from other types by presenting a general classification. Additionally, the chapter provides an overview of electrowetting devices and discusses a commonly observed phenomenon known as contact angle saturation within electrowetting systems. The concept of camouflage is also introduced and connected to the microfluidic system. As this thesis work primarily focuses on the development and characterizations of UHMWPE-based microfluidic and electrowetting approaches for adaptive camouflage across both visible and infrared spectrums, Chapter 1 provides a detailed introduction to the background and related information regarding these topics.

Chapter 2 presents a published work detailing the development and characterization of an innovative microfluidic device capable of adaptive multi-spectrum camouflage control, featuring a unique Macro-to-Micro interface design. It presents the results of characterization including SEM observation, FTIR and UV-Vis analysis, visual background matching analysis, average RGB colour matching analysis, colour pattern matching analysis, infrared reflectance appearance testing, and computerized edge detection analysis.

Chapter 3 presents a work detailing the development and characterization of an innovative low-voltage-driven electrowetting device designed for adaptive infrared camouflage control. The results are articulated through various techniques including digital tensiometer observations, infrared reflectance appearance testing, capacitance measurements, and infrared absorbance analysis. Notably, the presented electrowetting is characterized as nearly complete wetting without significant contact angle saturation effect.

Chapter 4 summarizes the major findings of all chapters of this thesis and suggests future directions for this research work.

1.3 Microfluidic Devices

Microfluidic devices and related technologies have been widely studied, researched, and fabricated over recent decades [1]–[3]. The history of research and fabrication of microfluidic devices dates back to the late 1970s [4], [5], primarily at Stanford University [6] and IBM [7]. The former focused on the development of a miniature gas analysis system based on gas chromatography on a silicon wafer. This chromatography system was fabricated by using photolithography and chemical etching techniques [4]–[6]. The system at IBM would go on to be used in inkjet nozzle production and was fabricated by using chemical etching techniques and versatile photolithographic micromachining for smaller dimensions [4], [5], [7]. These early applications of microfluidics were restricted by the materials and fabrication techniques which were silicon based and came out of integrated circuit manufacturing techniques [8]. Modern microfluidic technologies as known today were developed in the early 1990s [5], [9] as was their concept for being used as miniature biological laboratories. Since this time, the field has experienced exponential growth and diverged into many different areas[2], [3], [5]. Modern microfluidic device fabrication methods can be classified depending on the nature of processes applied such as chemical, mechanical, and other processes and the feasibility of these processes depend on the structural materials being used [3]. Common chemical processes for glass as an example include wet and dry etching [10]–[13]. While chemical processes are imperfect, since wet etching often involves hydrofluoric acid (HF) which is severely toxic [14], and while dry etching can avoid HF, it is much more time consuming and expensive for the equipment [12]. Mechanical processes that can be used for alternative structural materials like polymers include micromachining, micro-milling, xurography and laser etching. Of these techniques, xurography, which patterns thin layers by using a razor blade is a low-cost less time consuming process, and more importantly does not require a clean-room conditions [15]–[19]. The schematic representation of the xurography technique for microfluidic device preparation is illustrated in Figure 1. Some general microfabrication material removing techniques applicable to microfluidics have been summarized by a 2021 review article [3].

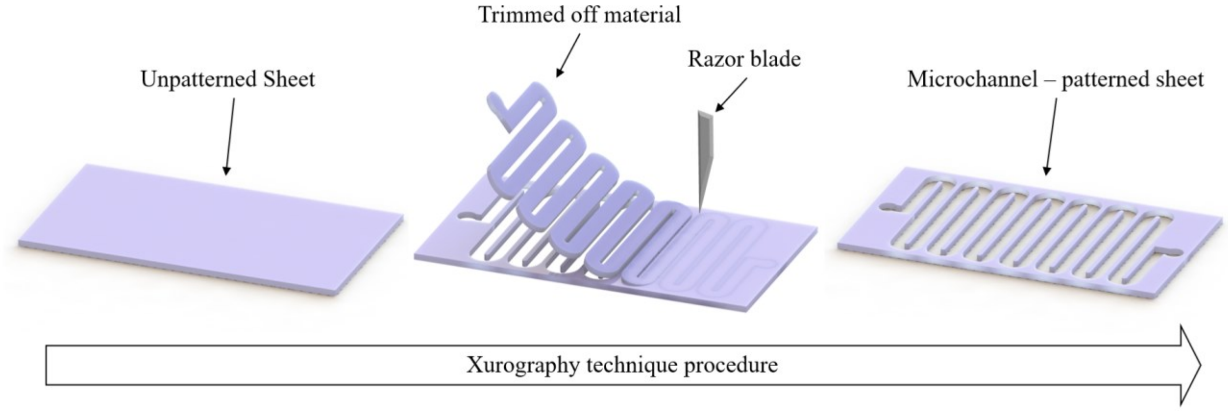

Figure 1. Demonstrates the schematic processes of xurography for microfluidic device preparation. The microchannel – patterned sheet is fabricated by trimming the shape of channel off the original sheet using razor blade.

1.3.1 Device Applications

The majority of reported microfluidic applications have been in support of bioscience (drug discovery, cell studies, analysis and diagnostic tools etc.) and fall under a theme of Lab-on-a-Chip (LoC) devices. The benefits of such device if it functions as desired could be significant as if the scale of the system could be shrunk, the consumption of reagents and samples can also be reduced, and the fabrication cost is decreased [1], [5], [9], [20] in an analogous fashion to the reduction in cost of computer processing power over decades. LoC microfluidic devices have been developed for many applications under the comprehensive biochemical and biomedical subjects, including chemical material detection [21], compositional analysis [22], biomedical reaction analysis [23], and even cell manipulation [24]. LoC systems are not the only application of microfluidics however, and microfluidic devices have also demonstrated promising results in optical areas [25], [26] where the devices showed the capability to act as a variable focusing liquid lens based on electro-wetting for curvature sensors [27]. By incorporating multiple microfluidic plugs into interior fiber microchannels, a class of active, tunable optical fiber can be fabricated [28]. A flexible multicolor display was developed based on microfluidic recently [29].

1.3.2 Device Materials

The range of material selection of microfluidic devices is diverse due to the broad applications. Silicon was used for the very first devices [6], [7] and Ecoflex silicone rubber has been used for a soft machine with microfluidic channel [30]. Silica gel can also be used to fabricate microfluidic device for more exotic applications in display purposes [31]. Poly(dimethylsiloxane) (PDMS) has emerged as one of the most actively developed foundational polymers for microfluidics owing to it ease of use, optical clarity and ability to be replicated with nm accuracy from a variety of mold materials [25], [29], [32]–[36]. Thermoplastic polymer materials including poly(methyl methacrylate) (PMMA), polycyclic olefin (PCO), polycarbonate (PC), polystyrene (PS), and polyethylene (PE) are also widely used for their relatively low costs and range of visible or thermal properties [35], [37]–[39]. Many other materials exploited in microfluidic devices can be found in various review articles [3], [40], [41].

1.3.3 Macro-to-Micro Interface

Although there have been many applications and development of microfluidic systems, a critical concern still exists as the connection between the microfluidic components and the rest of the world (macro) [42]. It is also referred to Macro-to-Micro interface, interconnect, or world-to-chip interface [42]–[45]. The interface is typically the least reliable components of a LOC microfluidic device and has huge impact on the overall performance [46]. Moreover, the processes to integrating fluidic connections typically contributes significantly to the overall cost of the device [42], [46]. Multiple interfaces were developed including wells, integrated interconnectors, module interfaces, and other systems, and detailed information can be found in a comprehensive review article[42].

1.4 Polyethylene

Polyethylene (PE) has the simplest structure of any polymer and is also the largest volume produced plastic currently [47]–[49]. The official polymerization of ethylene ($\mathrm{CH_2 = CH_2}$) into solid polyethylene ($\mathrm{(-CH_2 - CH_2 -)}$) was first achieved in 1933 by Reginald Gibson and Eric Fawcett, who worked in the laboratories of Imperial Chemical Industries, Ltd [50]–[52]. A subsequent patent was filed in 1936 and accepted in 1937 [53]. All the related commercial PE since then was fabricated by the high-pressure process introduced in this patent, and these PEs were recognized as low-density polyethylene (LDPE). However, in the mid-1950s, two alternative paths [48] (Phillips Catalyst [54], [55] and Z-N Catalyst [56], [57]) were developed which reduced the formation pressure and temperature. Through these processes, polyethylene can be formed at lower temperatures and pressures which resulting in a harder polymer with higher density and higher melting points. This type of polyethylene is also known as high density polyethylene (HDPE). Since then, more types of PEs have been synthesized based on different improved catalysis methods [58]–[60]. Owing to the various types of PE, it is typically classified based on the density and melt index (MI or melt flow index) [47]. Some typical PE types include LDPE, HDPE, linear low-density polyethylene (LLDPE), and ultra high molecular weight polyethylene (UHMWPE) [61]. Due to its versatile properties, PE has been used for packaging films, containers, pipes [47], clinical purposes [62], fibers, insulators, personnel armours [63], and almost every other aspect of daily life.

1.4.1 Ultra High Molecular Weight Polyethylene

UHMWPE is a subset of polyethylene family, distinguished by its extremely long chains of polymer unit which has a molecular weight over $3 * 10^6 \mathrm{g/mol}$ [64], [65]. It served as a type of high-performance specialty polymers with unique properties such as high wear resistance, corrosion resistance, mechanical resistance, and low friction [61], [66]–[69].

A brief comparison between several PEs is presented in Table 1 which reveals some vital features of UHMWPE such as no flow at melt condition and a relatively high melting temperature.

Table 1. General classification of polyethylene with physical properties, this table is adapted from [64].

Polyethylene	MFI (g/10 min)	Molecular weight M_w ($\times 10^6$ g/mol)	Melting Temperature (°C)
HDPE	0.1 – 100	0.1 – 0.5	125 – 135
HMW HDPE	0.01 – 0.1	0.2 – 1.0	130 – 135
UHMWPE	No Flow	> 3	135 – 148

1.5 Electrowetting

Electrowetting systems and related technologies have been widely researched, fabricated, and developed for over a century from 1875 when Gabriel Lippmann developed the theory of electrocapillarity in his PhD thesis [70], [71]. The electrocapillarity effect indicates that adding external electrostatic charge across an interface can greatly alter the capillary forces, which is the basis of electrowetting [72], [73]. Multiple works were conducted since then including the early-stage liquid droplet actuation by external signals [74]–[76], mercury droplet manipulation utilized in displays and optical switches (also the origin of the terminology of “electrowetting”) [77]–[79], and more investigations on different electrodes [79]–[81]. However, these studies relied upon direct contact at the droplet – electrode interface, which was fundamentally different from modern electrowetting systems, and far from practical applications [73], [76], [79]. The main obstacles of direct contact configuration were the involvement of toxic heavy metal – mercury [82], and the electrolytic decomposition of liquid droplet upon adding external voltages above several hundred millivolts [72], [79]. Another groundbreaking configuration setup was proposed by Berge to solve the decomposition [73], [83], which implemented a thin layer of insulator film on the electrode to separate the droplet from direct electrical contact. This was known as electrowetting on insulator coated electrodes (EICE), or in well-known modern terminology as electrowetting on dielectric (EWOD) [79]. Since EWOD was developed, electrowetting technologies have improved rapidly. Due to the demand of precise manipulations of liquid droplets and the trend of miniaturization, multiple practical applications were developed [71], [79]. These applications include liquid lenses [84]–[87], electronic displays [88]–[91], and multiple lab-on-a-chip microfluidic assay devices [92]–[94]. The commercialization status of EWOD systems was also reviewed recently [95]. More detailed information about the electrowetting developments can be found in other reviews [71]–[73], [76], [79].

1.5.1 Contact Angle Saturation

The electrowetting contact angle behaviour can be modeled using the simplified version of Lippmann – Young's equation as [72]:

$$\cos\theta(U) = \cos\theta_{\mathrm{Y}} + \frac{CU^2}{2\sigma_{\mathrm{lv}}}$$

where θ is the contact angle of the liquid droplet, θ_{Y} is the Young's angle (*i.e.*, the equilibrium angle when no voltage applied), σ_{lv} is the interfacial tension between the liquid droplet can vapour, note that the ambient phase was denoted as "vapour" for simplicity, the ambient can be another immiscible liquid with the droplet, C is the capacitance per area of the dielectric layer and U is the applied voltage. The relationship between θ (contact angle of the liquid droplet) and U (applied voltage) is described as parabolic function in the equation. The droplet contact angle obeyed the relationship for small voltages, however, as the applied voltages goes larger the contact angle often appears to deviate from the equation's predicted value and saturates [96]–[99]. This phenomenon is also known as Contact Angle Saturation (CAS). For some generic electrowetting system including oxide-cover with nanometer scale thin layer of hydrophobic coating, the saturation value can be as high as 70° - 80° [100]. Multiple saturated electrowetting systems were documented with the contact in angle of 30° - 95° [101]. The nature of CAS is still under investigation, yet multiple models have been built to discuss and analyze the mechanism [100], [102]–[104]. However, these efforts are beyond the scope of this work.

1.6 Camouflage

Camouflage is a vital ability, serving as a means of hiding from potential threats. Many animals exhibit natural camouflage skills, evolving a variety of inherent defensive color patterns [105], [106]. However, animals with fixed body colorations face limitations, especially when their static colors cannot adapt to changing backgrounds as they move [107]. Compared to fixed body color, a more remarkable mechanism is rapid adaptive camouflages that can be achieved by cephalopods, which can change their visual appearance in seconds [107]. Similarly, camouflage is crucial for soldiers in the military fields [108], [109] as it will make detection or recognition more difficult [105]. The pattern of modern military camouflage is designed digitally [110]. However, typical military camouflage faces similar drawbacks as animal's fixed protection colors, the pattern itself is unchangeable [111]. The conventional solution has been to provide soldiers with multiple uniforms, each with different patterns and colors suited for various backgrounds [112]. Modern military camouflage textiles are typically olive, green, khaki, brown and black [113]. Many efforts have been made to improve the camouflage performance of military textiles since the detection system equipped at the beginning of the 20th century [114], [115]. Apart from regular visible camouflage, infrared camouflage is also highly desired due to the use of surveillance equipment that is sensitive to infrared radiation [113]. The wavelength range of detection are 3-5 and 8-12 micron which are transparent to infrared in Earth’s atmosphere [116]. different approaches was reported by using nanostructured polymers that alternate reflection, using thin film to control emission, manipulate diffraction, and tuning emissivity through micro-scale designed metamaterial [117]–[121]. Moreover, various microfluidic devices have been developed for infrared camouflage. These devices utilize the programmable microfluidic strategy to manipulate infrared lights [38] and alter temperature to achieve camouflage [30].

Chapter 2

Low-Cost and High-Speed Fabrication of Camouflage-Enabling Microfluidic Devices using Ultra High Molecular Weight Polyethylene

2.1 Introduction

Microfluidic devices and related technologies have been widely studied, researched, and fabricated for decades [1]–[3]. The history of research and fabrication of microfluidic devices dates back to the late 1970s [6], [7]; however, the progress in the early stages of microfluidics was restricted by materials (silicon was used as a basic material early on) and fabrication techniques (photolithography, micromachining, and thin-film techniques) [8]. Despite these limitations, modern microfluidic technologies were developed in the early 1990s [3], [5], [9]. Since then, the microfluidics field has experienced substantial growth and diverged into various areas including biochemical, biomedical and optical areas [122]–[124].

Camouflage is a crucial topic in the field of optics, as it provides a means of hiding from danger. Some animals show camouflage skills in the nature by evolving a range of defensive colour patterns including fixed and adaptive body coloration [105], [106]. The limitation of fixed body coloration in an animal is evident as the color cannot adapt to the changing background while in motion [107]. In contrast, cephalopods possess a remarkable ability to achieve rapid adaptive camouflage by altering their visual appearance in a matter of seconds [125, pp. 145–163]. Similarly, camouflage plays a crucial role in military operations, making it harder for soldiers to be detected or recognized [108], [109]. The patterns of modern military camouflage is often designed digitally [110], [126] with a fixed coloration patterns. Since the patterns are unchangeable, soldiers face difficulty in adapting to different environments or unpredictable situations [111], [112]. Researchers have been investigating innovative methods of adaptive camouflage utilizing microfluidic technology [114]. In this approach, a colored liquid fills a specific microfluidic pattern, which can rapidly alter its appearance to blend in with the surrounding environment. A type of liquid colour-changing lenses with a microfluidic channel was developed with the capability of vision protection, camouflage, and optical filtering [25]. However, the material used was poly(dimethylsiloxane) (PDMS) which is not IR transparent and, thus, limited its application for visible camouflage. To the author's knowledge, only one microfluidic device that used PE was fabricated to manipulate both visible and infrared appearance. This device was fabricated using levels of channels combined by thermocompression molding [38]. Although the device achieved the proposed goal, the mold manufacturing required chemical etching of a stainless-steel sheet which adds extra complexity on the device fabrication. Moreover, many of the chemical etchants are highly corrosive, toxic and pose a risk to human health and the environment [30], [38], [114].

Microfluidic devices capable of achieving color-changing camouflage followed specific critical design and fabrication rules for material selection. In particular, only visible transparent or semitransparent materials should be used as the surface (top) layer of these devices to enable the efficient manipulation of fluids and enable the desired color-changing effects [30], [38], [127]. Most microfluidic materials have been used to fabricate transparent microfluidic devices in the visible spectrum. Silicon was used for the very first devices [6], [7]. Ecoflex silicone rubber was used for a soft robot with microfluidic channels to create a camouflage system [30]. Silica gel can also be used to fabricate microfluidic devices [31]. In addition, PDMS is a mineral-organic polymer (a structure containing carbon and silicon) which has been one of the most actively developed and been a foundational polymers for microfluidics [25], [29], [32]–[36]. Thermoplastic polymer materials such as poly(methyl methacrylate) (PMMA), polycyclic olefin (PCO), polycarbonate (PC), and polystyrene (PS) can also be alternative materials to fabricate color-changing microfluidic devices as they are optically transparent [37]. However, these different materials are opaque to infrared light. On the other hand, Polyethylene (PE) is transparent from the visible region to the end of mid-IR [35], [38], which makes it a promising candidate for combined visible and IR camouflage.

The selection of fabrication methods for camouflage microfluidic devices is restricted by the need to ensure both simplicity and reliability while maintaining optical transparency and precise control over the microchannel geometry [40], [128]. The traditional microfluidic device fabrication methods can be classified into two main categories, material removal techniques (subtractive) and material depositing techniques (additive). However, material deposition usually requires the material can be applied in desired amounts at specific locations; the material needs to be transportable and can turn into a solid at that location [11]. On the other hand, material removal techniques have fewer requirements regarding the material properties; therefore, removal techniques have been more generally applied [11]. Besides this classification in terms of material addition and removal, the fabrication methods can also be identified by the processes, including chemical processes, mechanical processes, and laser-based processes [3]. More information can be found in detailed reviews published on these fabrication processes [3], [10], [11]. Some processes are complex with multiple steps/operations involved (such as chemical etching); some of them such as laser-based processes are expensive; some of them such as electrochemical discharge machining can only be performed in a cleanroom facility; and many of them can suffer weak reproducibility, low resolution, material restriction, and slow rates [3], [10]. However, there is one mechanical process for material removal that is low cost and fast, and does not need to be performed in a cleanroom facility [3], [129]. Xurography, which is also known as razor writing, is an environmentally friendly and flexible process that uses a cutter to pattern features in a material. Xurography also has the ability to fabricate inexpensive and robust microfluidic devices in a short time [18], [130].

Besides channel manufacturing, it is also very important to connect the micro-structured device to the outer world, which is often referred to as the macro-to-micro interface. Since the interface between the microfluidic device and the peripherals (tubing) is typically the least reliable components of a microfluidic device, getting interconnection to be robust has a significant impact on the overall performance. Moreover, the processes used to integrate fluidic connections typically contribute to the overall cost of the device [42], [46]. Further work related to microfluidic interfaces can be found in the following review article [46].

In this study, we demonstrated a fast (few minutes) and inexpensive (less than 0.09 Canadian dollar per piece) fabrication technique for a multilayered microfluidic device with adaptive camouflage capabilities. It is featured with a microchannel structure and is based on a single material, ultra high molecular weight polyethylene (UHMWPE). This technique combines xurography (for the channel layer) and a thermal bonding process to complete the whole system. The process has the capability to be mass produced since the manufacturing can be standardized at scale by using punches or other cutting tools to produce complex channels from sheets. In addition, our fabrication technique shows the flexibility of the design as the size and aspect ratio of the microfluidic channel are fully tunable by different cutting patterns and choice of type of stock material. The microfluidic channel device demonstrates the ability to achieve visible camouflage by filling the channel with dyed liquids to match the microfluidic device to the background color as the device itself is semi-transparent and the transparency can be improved by simple surface treatment. In addition, the semi-IR transparent nature of polyethylene allows this design to also achieve IR camouflage by changing the IR appearance of an embedded metalized surface. The manufactured microfluidic devices were characterized in terms of the channel dimensions, IR & visible properties, and visible and IR camouflage effectiveness in matching different backgrounds.

2.2 Experimental Methodology

2.2.1 Materials

Ultra high molecular weight polyethylene film (UHMWPE, McMaster-Carr, Thickness = 0.004" and 0.01") and polyethylene tubing (PE tubing, McMaster-Carr, Inner Diameter = 1/16", Outer Diameter = 1/8") were utilized to fabricate the visible camouflage microfluidic channel device. Food dyes (E-Kongton, China) were used to prepare aqueous dyed solutions using deionized (DI) water. The concentration of the food dye in DI water was 20% weight ratio. An ultra thin multi-layered metalized (aluminium) polyethylene sheet used in food packaging (Cleaned Cheetos Bugles Package Bag) was added to the original visible camouflage microfluidic device to obtain an IR camouflage device. DI water was used as the circulation fluid inside the channel. All the materials were used without modifications and can be considered commercial off-the-shelf (COTS) components.

2.2.2 Equipment

A craft cutter (Silhouette Cameo 4, China) was used to fabricate the microchannel layer. The cutting pattern can be designed either by the Cameo 4 studio software or the drawing file can be imported from an engineering drawing software (SolidWorks was used for our design). The heat bonding of the layers of the microfluidic device was performed with a hot plate (HS40A Scientific Programmable and Stirring Hot Plate, Torrey Pines, USA) and a T-shirt heat press. A setup with a syringe was developed to circulate the liquid within the microfluidic channel. An oven (Isotemp™ Model 281A Vacuum Oven, Fisherbrand™, USA) was used as a thermal background for the infrared transparency demonstration. A 3D printer (Ender 3, Creality 3D, China) heating bed was used as a thermal source for the infrared reflection characterization. The cross-section of the microfluidic channels was analyzed using a Field Emission Scanning Electron Microscope (FE-

SEM, Zeiss, Oberkochen, Germany). The infrared and visible spectra of the microfluidic devices were measured using attenuated total reflectance Fourier transform infrared (ATR-FTIR, Agilent Cary 600 series, Canada) and UV-Vis spectrophotometer (Thermo Fisher Scientific GENESYS^{TM} 10, Canada), respectively. The pictures and videos of the microfluidic devices were recorded by smartphone (iPhone 13 Pro Max, USA).

2.2.3 Preparation of the Microchannel Layer

The microchannel layer was prepared by cutting a thin sheet of 0.004” UHMWPE with a blade using the craft cutter. In this design, the height of the microfluidic channels was mainly controlled by the thickness of the PE sheets used for each layer. The UHMWPE sheet was attached to a sticky mat for the cutting operation. The cutting setting was optimized for each thickness of PE sheet in order to achieve the highest accuracy of cutting along with an acceptable speed. More information on the cutting settings can be found in Table A1. After cutting the UHMWPE sheet, the layer was transferred to a piece of double-sided polyester tape (Flexmount DF051521). By removing the interior cut portion from the tape, the channel structure was achieved.

2.2.4 Fabrication of the Microfluidic Device for Visible Camouflage

The fabrication process of the visible camouflage microfluidic device was based on thermal bonding as shown in Figure 2. The order of in which the layers were bonded matters as the microfluidic channel must have at least one inlet and one outlet for the connection tubes. The overall fabrication process consisted of three parts: the formation of the bottom layer (Figure 2a – d), which had the channel structures; the formation of the top layer (Figure 2e-h), which had the inlet/outlet tubes; and the final assembly of the two layers (Figure 2i – j).

The formation of the bottom layer started by placing a polyester sheet (which acted as a high temperature tolerant release layer) on a hotplate set at a temperature of 180°C. An UHMWPE sheet was placed on top on the polyester sheet. A silicone roller was used to ensure complete melting of the UHMWPE sheet (Figure 2a). Convenient for this process, UHMWPE barely flows in its molten state due to the high molecular weight and is more of a rubbery solid than liquid; therefore, it maintained its dimensions and relative tolerances despite being above its melting point. Thereafter, the microchannel structure (prepared in the previous section) was placed on top of the heated UHMWPE sheet and rolled a few times to ensure good bonding between the channels and the bottom layer – detectable once both surfaces looked transparent with no visible voids (Figure 2b & c). Since the double-sided tape had a higher heat resistance than the UHMWPE sheet, it did not melt during this step and was easily peeled off after cooling. A permanent bond was achieved between the channel structure and the bottom sheet, and the PE 2-layer assembly remained adhered to the polyester sheet (Figure 2d).

The formation of the top layer began in a similar way as for the bottom layer by placing a polyester sheet on the hotplate at 180°C then rolling an UHMWPE sheet on top of it until complete melting (Figure 2e & f). For heat bonding the PE tubes to the UHMWPE sheet, an extra layer of polyester sheet was required: it had two holes cut using a hole puncher (Figure 2e & f). The distance between the holes was the same to the distance between the inlet and the outlet of the microfluidic channel; the diameter of the holes was slightly larger than the PE tube (by less than 1mm) to ensure that the tubes can go through the holes in the polyester sheet. This polyester sheet with holes was then placed on top of the PE sheet and rolled with the silicone roller to form a sandwich structure so that the UHMWPE sheet was in between the two polyester layers. Thereafter, two 1-inch-long PE tubes were inserted through the holes in the polyester sheet and press melted to the UHMWPE layer. The bonding time between the tube and the UHMWPE sheet was ~ 5 seconds, which was enough to ensure complete bonding. The sandwiched UHMWPE with the tubes was cooled down and the bottom polyester layer was removed (Figure 2g). Finally, a needle was used to punch through the PE tube and the UHMWPE layer, forming the inlet/outlet holes (Figure 2h).

The final step was to melt the bottom layer with the top layer on the hotplate at 180℃. The top layer (with the polyester sheet) was placed on the bottom layer with the two tubes aligned with the inlet and outlet positions in the microfluidic structure in the bottom layer (Figure 2i). A silicone roller was used to ensure a complete bonding between the layers. After removal from the hotplate and cooling down, the polyester layers were removed, which completed the fabrication of microfluidic device (Figure 2j). If the polyester support were not used in the fabrication process, large membranes over reservoirs and channels would frequently buckle and self- adhere in undesirable locations (See Figure A1).

The effectiveness of the fabrication method was evaluated by fabricating microfluidic channels with different thicknesses and heights. The channels were categorized based on their width into W1 (0.5mm), W2 (1.0mm), and W3 (2.0mm), while the height of the channels was categorized into H1 (0.004 inches), H2 (0.008 inches), and H3 (0.012 inches). The channel height for W1, W2, and W3 was fixed at 0.004 inches. The channel widths for H1, H2, and H3 was fixed at 1.0mm. Channel heights of 0.008 inches, and 0.012 inches were achieved by thermally bonding two and three layers of the 0.004 inch thick sheets, respectively, prior to cutting the channels.

2.2.5 Fabrication of the Microfluidic Device for IR Camouflage

The fabrication process of the IR camouflage microfluidic device was very similar to the visible one (Figure 2). The main difference is that the IR camouflage device uses an additional metallized layer between the microchannel layer and the bottom layer. This was achieved by embedding a metalized polyethylene laminate film from food packaging between a 0.004” UHMWPE sheet and a 0.01” UHMWPE sheet (that served as a harder back layer to support the package bag) by using the T-shirt heat press set to 148.9℃. The metal side was facing upwards and placed in between two PE sheets; the 0.004” UHMWPE was used as the top layer, and the 0.01” UHMWPE was used as the bottom layer to form a sandwich structure. When bonded between two PE sheets, the package bag was flattened and kept mechanically stable for the following xurography process. For this operation, the UHMWPE-metallized layer-UHMWPE sandwich structure was cut by the craft cutter. For this cutting, the depth of the blade was precisely controlled so that only the top UHMWPE layer was cut without penetrating the metallized layer below. More information on the cutting settings can be found in Table A1. Next, the cut-out material inside the channel was removed. The top layer with the connection tubes was prepared as shown in Figure 2e-h. For the assembly of the two layers, the heat bonding temperature was lowered to 150℃. Since the package bag itself is an ultra thin multi-layered metalized sheet and the package bag tended to shrink due to polymer internal stress at temperatures above 150 °C. An image of the microfluidic device with an incorporated metalized sheet can be found in Figure A2.

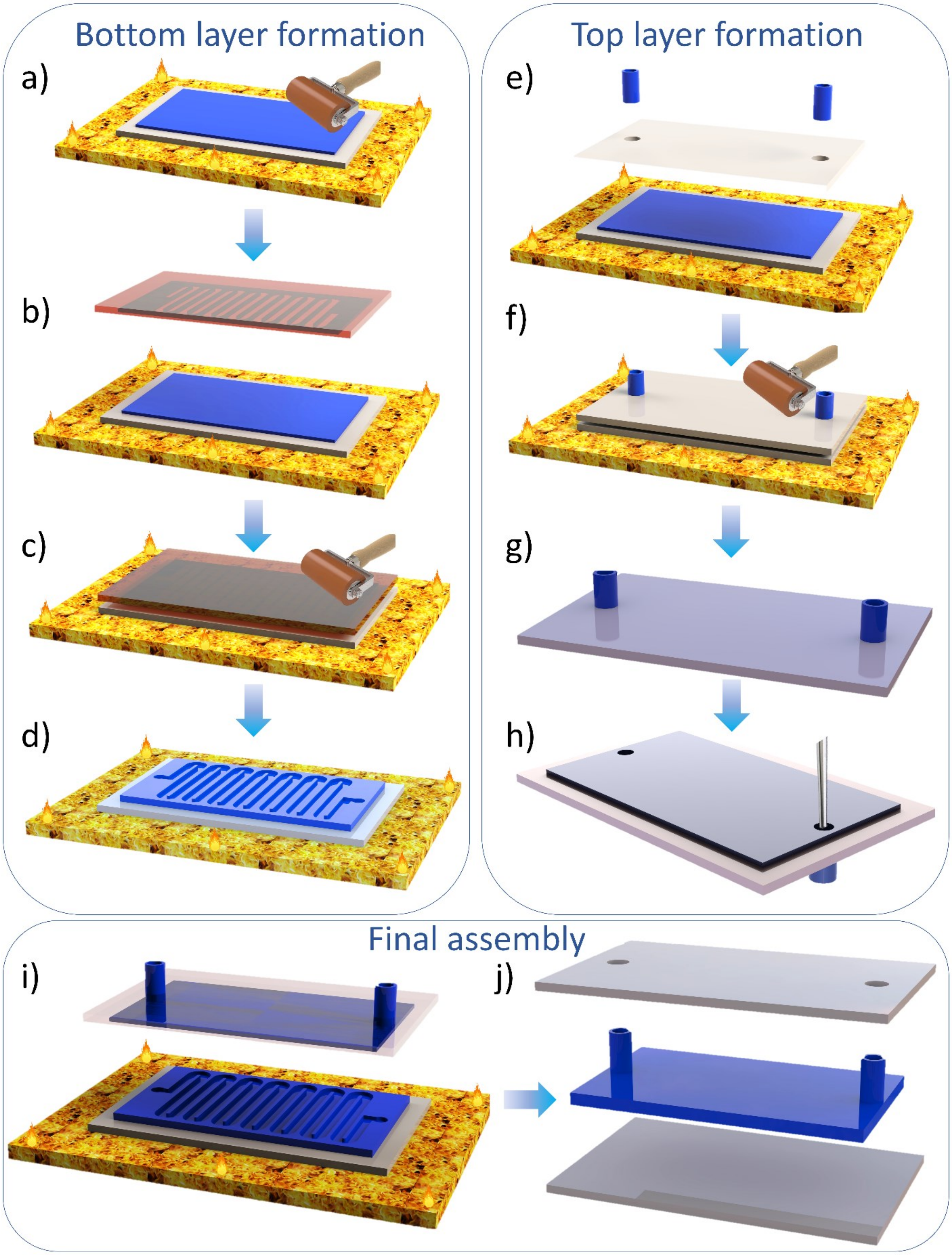
Bottom layer formation
a)
b)
c)
d)
Top layer formation
e)
f)
g)
h)
Final assembly
i)
j)

Figure 2. The fabrication steps of the microfluidic devices including the top layer, the bottom layer, and the final assembly: (a) melting an UHMWPE sheet on a polyester substrate at 180°C; (b) & (c) bonding and rolling the taped UHMWPE layer with the microchannel structure on the melted UHMWPE sheet; (d) peeling off the double-sided tape from the channels, which results in the formation of the bottom layer; (e) melting and sandwiching an UHMWPE sheet between two polyester sheets with the top polyester layer having holes for the inlet outlet tubes; (f) melting PE tubes through the holes of the top polyester sheet to the sandwiched UHMWPE sheet and rolling the structure to ensure complete melting; (g) & (h) removing the bottom polyester and piercing holes through the PE tubes to form the inlet/outlet channels; (i) & (j) melting the top and bottom layers to form the final microfluidic device.

2.2.6 Characterization

2.2.6.1 Microchannel Structure and Dimensions

The cross-section images of the microchannels with different dimensions were examined by field emission scanning electron microscopy (FE-SEM,). The specimens were prepared by cutting the UHMWPE sheets with the microchannels using stainless steel scissors. The microchannel samples were mounted on SEM stubs with carbon tape and coated with a gold layer (~2 nm, Denton gold sputter) prior to SEM imaging.

2.2.6.2 Microfluidic Device Visible Camouflage Tests

The visible light camouflage tests were performed at the outdoor scenes of Edmonton, Canada during fall season (September and October 2022). Several most representative background colors were selected: green from grass, red from maple leaves and bricks, yellow from withered leaves, and brown from dirt. The visible camouflage of the prepared microfluidic devices was characterized using the canny edge-finding algorithm, which is a popular and effective technique to detect edges and is widely used in computer vision for object recognition and detection [131]–[133]. The working principle of the edge-finding algorithm involves the conversion of an image into a grayscale version, followed by the use of two thresholds to detect a large gradient magnitude. The gradient magnitude at each pixel is then compared to its neighbors. Given that the gradient magnitude represents the change in intensity at a particular pixel, the color-change edge can be precisely detected [131]–[133]. The complete MATLAB code can be found in the supplementary information as Code 1. The visible camouflage of the devices was also characterized by evaluating the color matching performance. Two comparison regions were selected on the microfluidic devices and the environmental background. Upon filling the dyed liquid, the average color of the unfilled device region, filled device region, and background region were evaluated in terms of RGB values, which is a standard color space coding [134]. The average color RGB codes within each region are assessed and compared to demonstrate the color matching performance. The complete MATLAB code can be found in the supplementary information as Code 2.

2.2.6.3 Microfluidic Device IR Camouflage Tests

The IR camouflage tests were performed indoors using a FLIR E95 camera to look at microfluidics that were heated or reflecting a nearby thermal source. Figure 3 shows a schematic of the testing setup for both states unfilled (Figure 3a) and filled (Figure 3b). The emitted IR radiation on the microfluidic device experienced absorption, transmission, and reflection (specular and diffusive) by the top layer of the microfluidic device. Reflection tests were performed by exposing the microfluidic surface to a heat source (a 3D printer bed with a temperature of 100°C) with an incident angle of 45° and placing the camera at a reflecting angle of 45°. The angle was chosen so that the infrared radiation from the heat source can be reflected by the metal layer embedded in the device. Images of the microfluidic devices were recorded using the IR camera at different liquid filling stages.

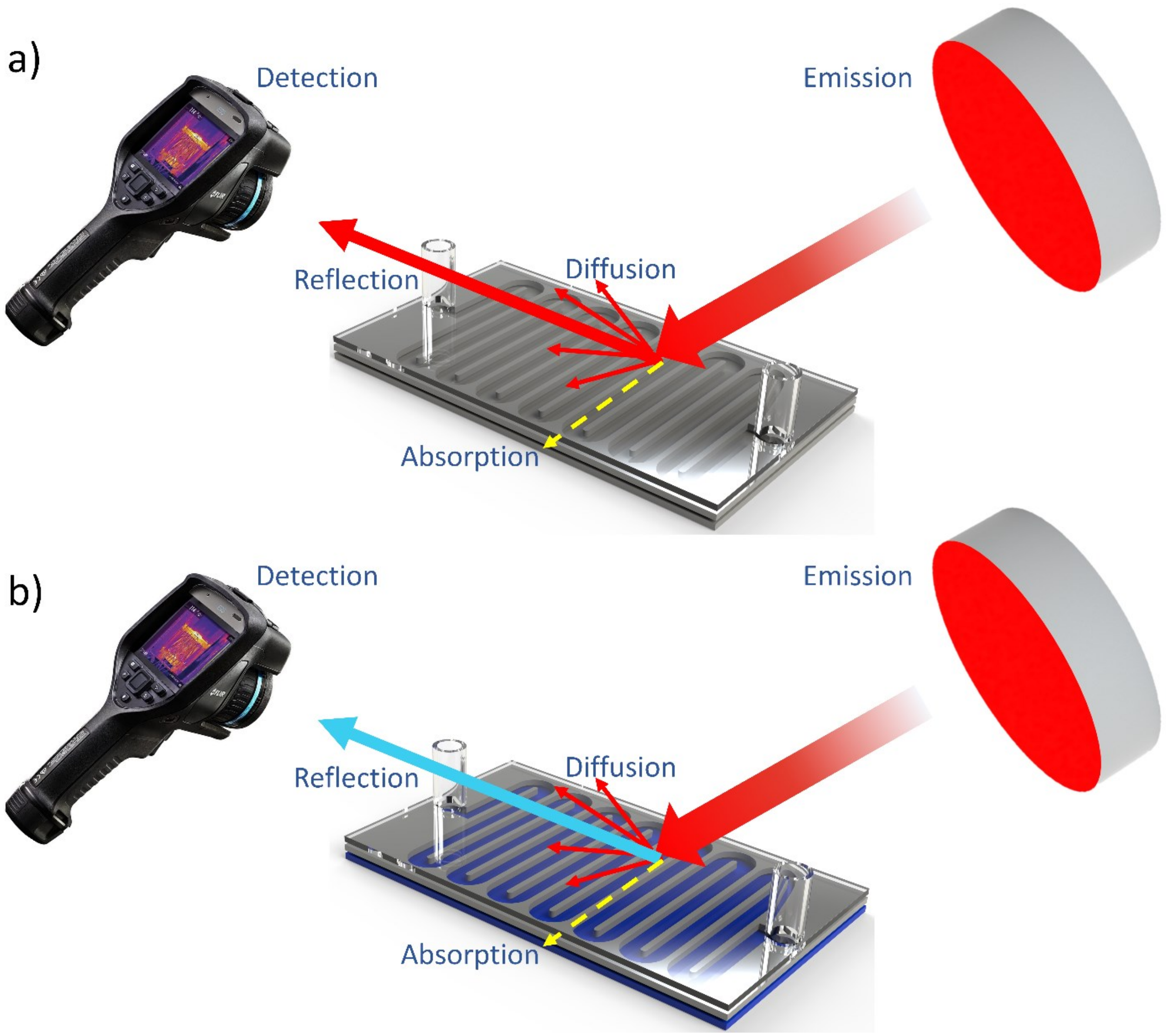

Figure 3. Schematic representation of the testing setup for the IR camouflage tests: (a) and (b) show the mechanism of the IR reflection and detection of the microfluidic surface in two states, non-activated (unfilled channels) and activated (channels filled with water).

2.3 Results and Discussion

The cross-sectional FESEM images of W1, W2, W3, H1, H2, and H3 devices are shown in Figure 4. The desired/achieved channel widths of W1, W2, and W3 were 0.50/0.6 mm, 1.0/1.3 mm, 2.0/1.8 mm, respectively, with a height of 100 µm ±9 µm. The desired/achieved channel heights of H1, H2, and H3 were 101.6/110.0 µm, 203.2/184 µm, and 304.8/264 µm, respectively. There was a slight deviation between the desired channel widths/heights and the values achieved. It was attributed to some inconsistencies in the craft cutting step and rolling pressure during thermal bonding. Since H2 and H3 required thermal bonding of multiple UHMWPE layers, the difference between the desired and the achieved thickness was higher than for H1, indicating that rolling during thermal bonding has a significant effect on the height. Upon closer examination of the channel edges, as illustrated in Figure 4 (H3), it was observed that the edges were devoid from any inter-layer extension, suggesting a complete permanent bonding between the three UHMWPE layers.

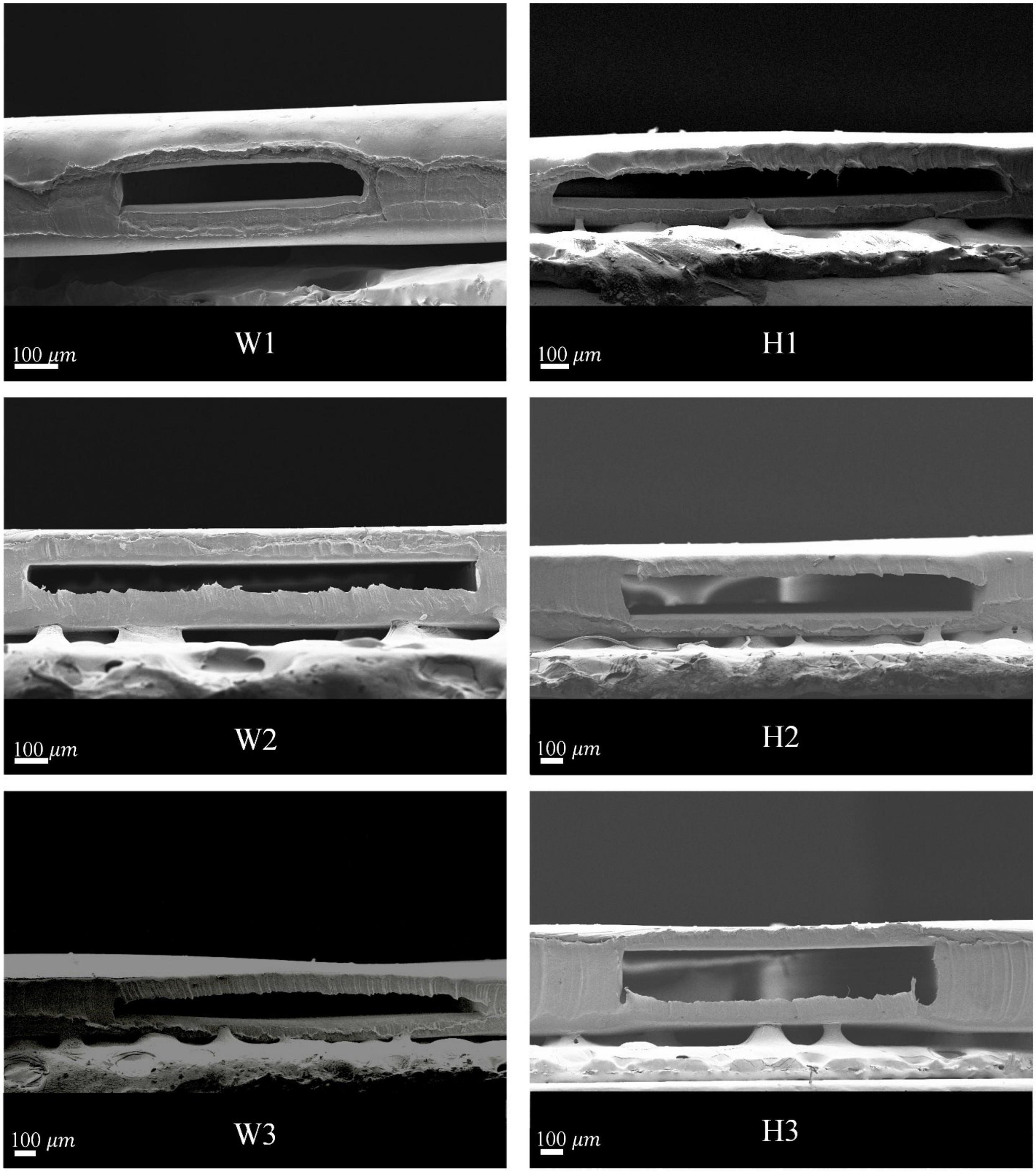

Figure 4. Cross-sectional SEM images for three different widths (W1, W2, and W3) and three different thicknesses (H1, H2, and H3) of the microfluidic device.

Figure 5a & b show the FTIR and UV-Vis transmittance and absorbance results for the UHMWPE sheets. Polyethylene is a semi-transparent material to infrared radiation because of the unique simplicity of its molecular structure [135]. It is made of a long chain of repeating units of ethylene monomers that are arranged such that there are relatively few chemical bonds that absorb/emit infrared radiation in the range of–3 – 14 µm. Therefore, IR passes through the material to some extent, making it semi-transparent as shown in Figure 5a. The visible transparency of the UHMWPE comes from the interaction between the visible light and the polymer molecular structure. The photons of the visible light do not have sufficient energy to excite the electrons in the PE molecules and cause them to absorb light. Therefore, visible light is transmitted through the material without being significantly absorbed (Figure 5b). Figure 5c shows a photograph of a microfluidic device placed on top of a heated University of Alberta (UofA) logo. The logo was made by cutting it from a metalized polyester film, which was then taped on top of a heated oven. The measured temperatures of the logo with and without the microfluidic device were 53 °C and 42 °C, respectively. As expected, there was a small drop in the apparent temperature due to the PE IR absorption. Figures 5d shows a picture of a microfluidic device placed on top of a UofA logo. Although the device consisted of 2 layers (0.008 inches in total) of PE, the UofA logo could be clearly identified. In order to achieve higher transparency, a simple surface treatment was introduced. Figures S3 & S4 demonstrated the results of different surface treatment temperatures by heat-pressing a 100 µm UHMWPE sheet on a smooth surface such as Kapton tape or polyester sheet. The treatment reduced the surface roughness and increased the visible transparency of the UHMWPE sheets. The visible appearance of the sheets changed from translucent to transparent.

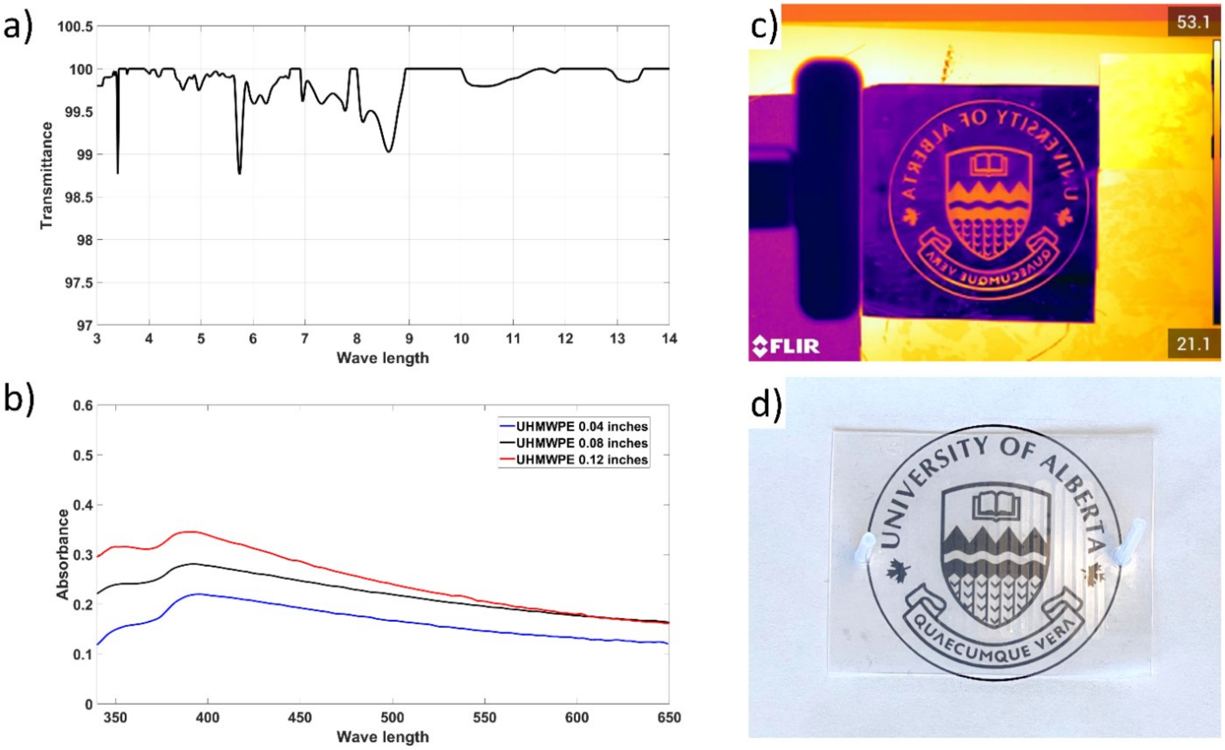

Figure 5. (a) Transmittance results for an UHMWPE sheet with a thickness of 0.004 inches over the range of 3 – 14 μm; (b) Absorbance results of UHMWPE sheets with different thicknesses (0.004, 0.08, and 0.12 inches); (c) IR images of a microfluidic device (W1) placed in front of a metalized heated UofA logo; (d) Microfluidic device (W1) placed on top of a printed UofA logo.

The visible camouflage characterization considered the color differences between the environmental background and the microfluidic channels in both states (filled and unfilled) as shown in Figure 6. The microfluidic devices were placed in front of various backgrounds, such as grass, dirt, leaf, and brick, to demonstrate their camouflage capabilities. The unfilled devices were easily visible and distinguishable against the background, but as the devices were filled with dyed liquid, they quickly blended in with the surroundings and became hard to detect. By changing the color of the dye, the microfluidic devices were able to adapt to different backgrounds. The effectiveness of the devices camouflage was more pronounced for grass (Video S1) and dirt (Video S2) backgrounds, as there was a close match between the intensity of the dyed liquid and the background. However, in the case of the leaf and brick backgrounds, the match with the device color was still acceptable but not as good as in the former two scenarios. The intensity and color of the dyes are not limited to what were used in this study and can be adjusted and modified as required. Therefore, adjusting the color and intensity of the dyed liquid can result in devices that are optimized for specific environmental conditions, therefore increasing their effectiveness in the field. The total time for the device actuation was typically less than 15 seconds; it was controllable by the change in the pressure applied on the syringe. With a larger pressure, the color changing was faster. By retracting the dyed liquid, the microfluidic device was able to return to a semi-transparent appearance. It is worth mentioning that our developed method for the permanent interface between macro-scale PE tubes and micro-scale channels ensured having robust and leak-free operations. All the prepared devices exhibited airtight and watertight features providing a strong and reliable seal that can withstand the high pressures and flows typically encountered in microfluidic.

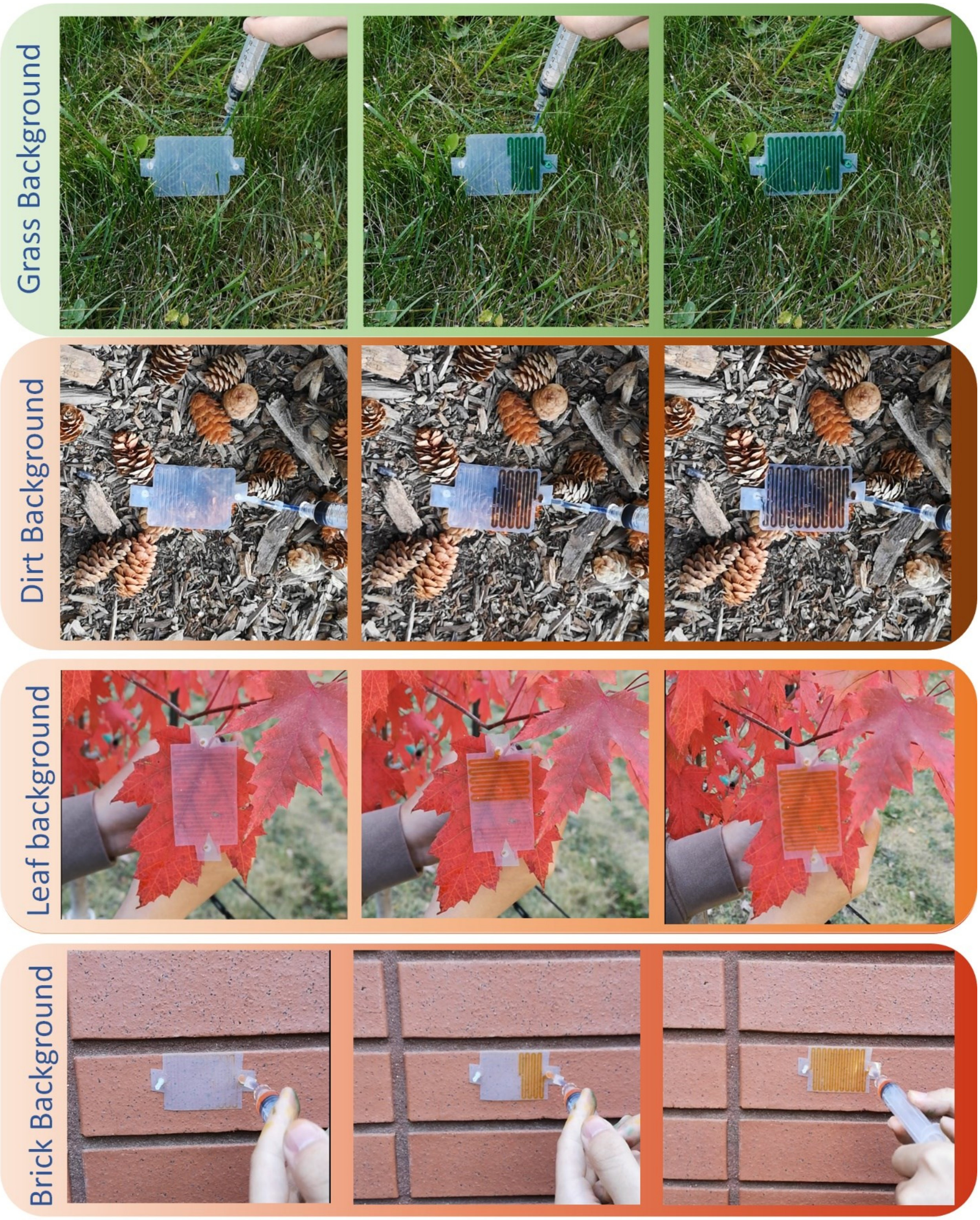

Figure 6. Images of microfluidic devices tested for their camouflage capabilities with different backgrounds (grass, dirt, leaf, and brick). The photos were captured in outdoor conditions on the University of Alberta campus.

The aim of visible camouflage is to conceal an object or individual when observed under visible light conditions [136]. This is achieved by reducing or eliminating the contrast between the object and the background, and by disguising the object's edges. Typically, this involves using colors and patterns that are similar to those found in the surrounding environment or by incorporating contrasting colors to break up the object's outline. To achieve effective concealment, it is necessary for camouflage devices to incorporate multiple colors, as natural environments are not comprised of a single color. Fortunately, our devices can easily be fabricated as a multi-input/output system to blend in multicolored background. Moreover, our fabrication process could easily be adjusted to fabricate devices with different channels patterns and shapes. By carefully designing the channel feature, the channel coverage ratio can be maximized with the rest surface areas including channel walls and device edges minimized. However, it is worth mentioning the presented visible camouflage demonstration focused on color-matching, shape-matching, and edge-hiding. The minimum feature size is not tested. Figure 7 shows three devices that are connected to correspond to distinct military camouflage patterns commonly utilized in various environmental conditions (Videos S3 and S4). These patterns were tailored to match the requirements of semi-arid climates (Middle East & Asia), leafy forests (North America & Europe), and naval environments [109], [137]. The multi-input/output microfluidic device demonstrated high matching capability in these diverse environments, making it a versatile and adaptable solution for visible camouflage. Notably, the device was not limited to a specific pattern, allowing it to be used across a wide range of environmental conditions. By providing a universal camouflage solution, this device could eliminate the need for multiple garments to match specific environments.

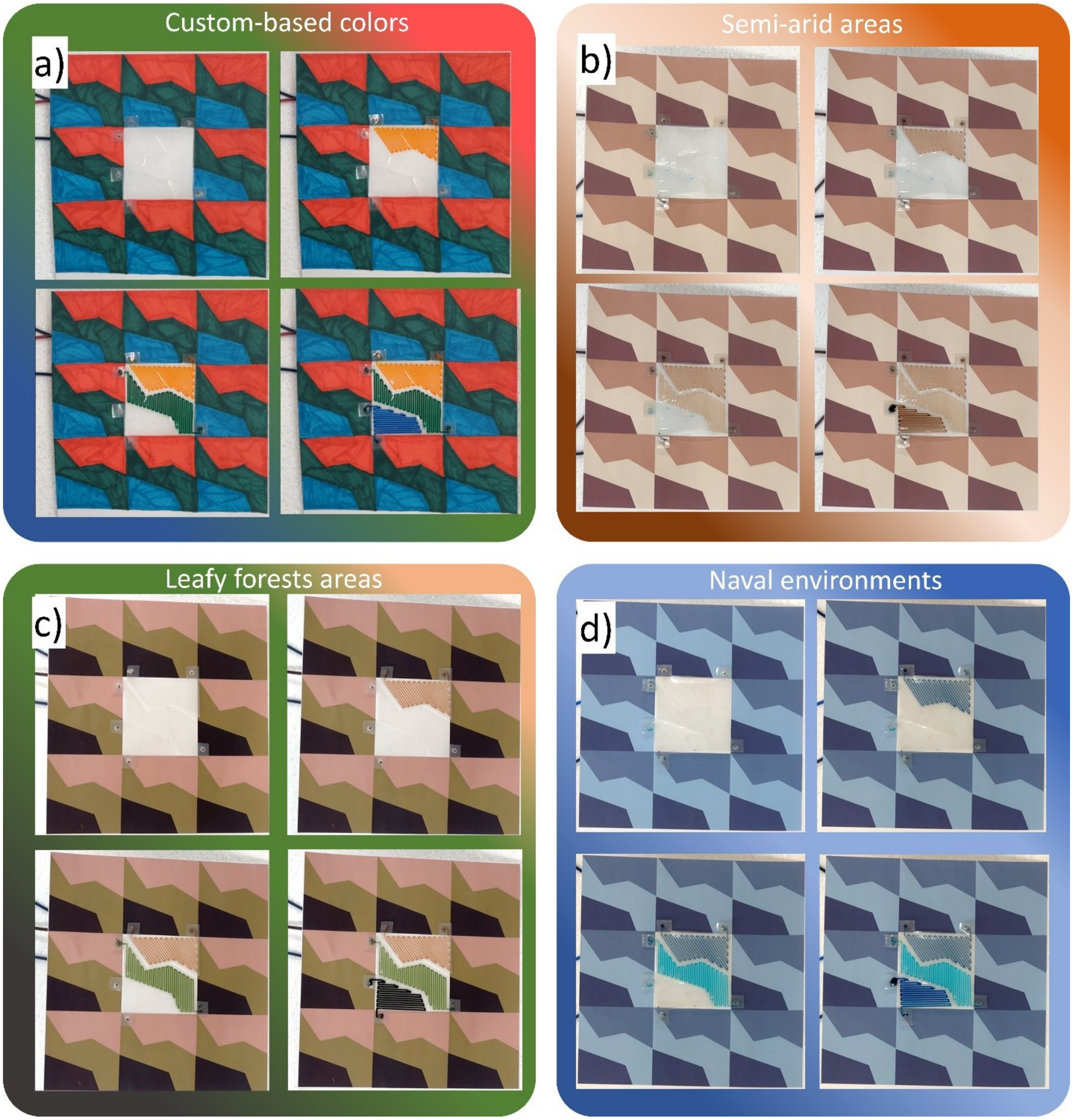

Figure 7. Multi input/output microfluidic devices for visible camouflage capabilities in multicolored backgrounds; The devices were tailored to match the colors and patterns of semi-arid climates (Middle East & Asia), leafy forests (North America & Europe), and naval environments.

To gain a deeper understanding of the visible camouflage effects of the microfluidic devices, further analysis was conducted using the canny edge finding algorithm. This algorithm is a commonly used image processing technique that can identify the edges of objects in an image

[133]. By applying this algorithm to images of the devices in various environmental settings, we assessed the effectiveness of the camouflage in terms of its ability to disguise or break up the outline of the device. The unfilled microfluidic devices showed up as black voids and were thus very distinguishable and detectable by the edge-finding algorithm. Interestingly, the filled devices merged into the background and were not recognizable. These results confirmed that the microfluidic devices were successful in reducing the contrast between the device and the background, as well as disguising the edges of the device as shown in Figure 8. Results for the leaf and brick backgrounds can be found in the supplementary information (Figure A5).

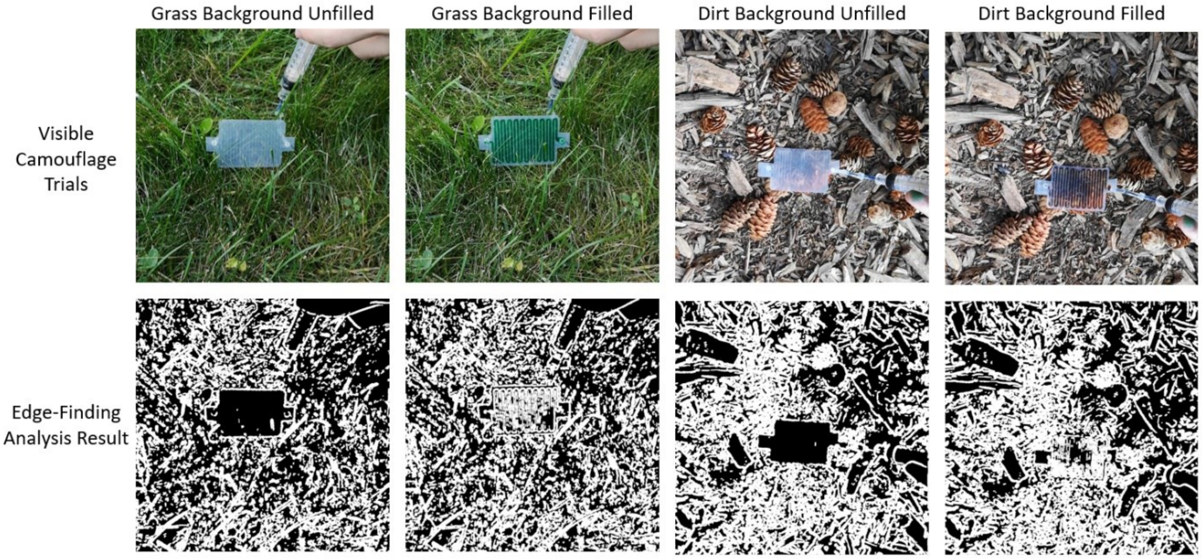

Figure 8. Canny edge-finding algorithm analysis results for selected trials (grass and dirt background). The first row provides images of the unfilled and dye-filled devices against the background. The second row is the results from MATLAB of the "Canny" edge finding algorithm. The white lines shows the edges detected by the code; the empty channels for both grass background and dirt background do not have detected edges inside. Some edges showed inside are most likely due to objects in front of the device. As for the filled channels, there are many detected edges inside the region of the device, which blurred the actual boundary between the device and background.

Besides disguising the edges and matching the shapes of the microfluidic device, the match of colors is also vital for camouflage evaluation. We assessed the color matching performance upon filling the channels by evaluating the average RGB color values of the microfluidic device and the background. The results are presented in Figure 9, where the first and second columns demonstrate the labeled environmental backgrounds and microfluidic devices in both states (filled and unfilled). The red square represents the selected background region, while the green square represents the selected microfluidic device region. The third column presents the analysis results of the average color RGB values for the unfilled device region, filled device region, and background region. The bar charts separately display the red, green, and blue values to show the matching trend as the device was filled. RGB codes have a range of [0-255], where 0 represents black, and if all three R, G, and B values are at their maximum of 255, it appears as white. Under normal conditions, the unfilled device appears visibly translucent (whitish), thus the RGB codes for the unfilled device have relatively high values. As shown in Figure 9, filling the device results in its RGB values to have a significant trend of matching to the background RGB values. The RGB values of the filled devices and background were similar, indicating a similar color. These results support the successful matching of the microfluidic devices with the background color. The detailed RGB values can be found in the supplementary information in Figure A7.

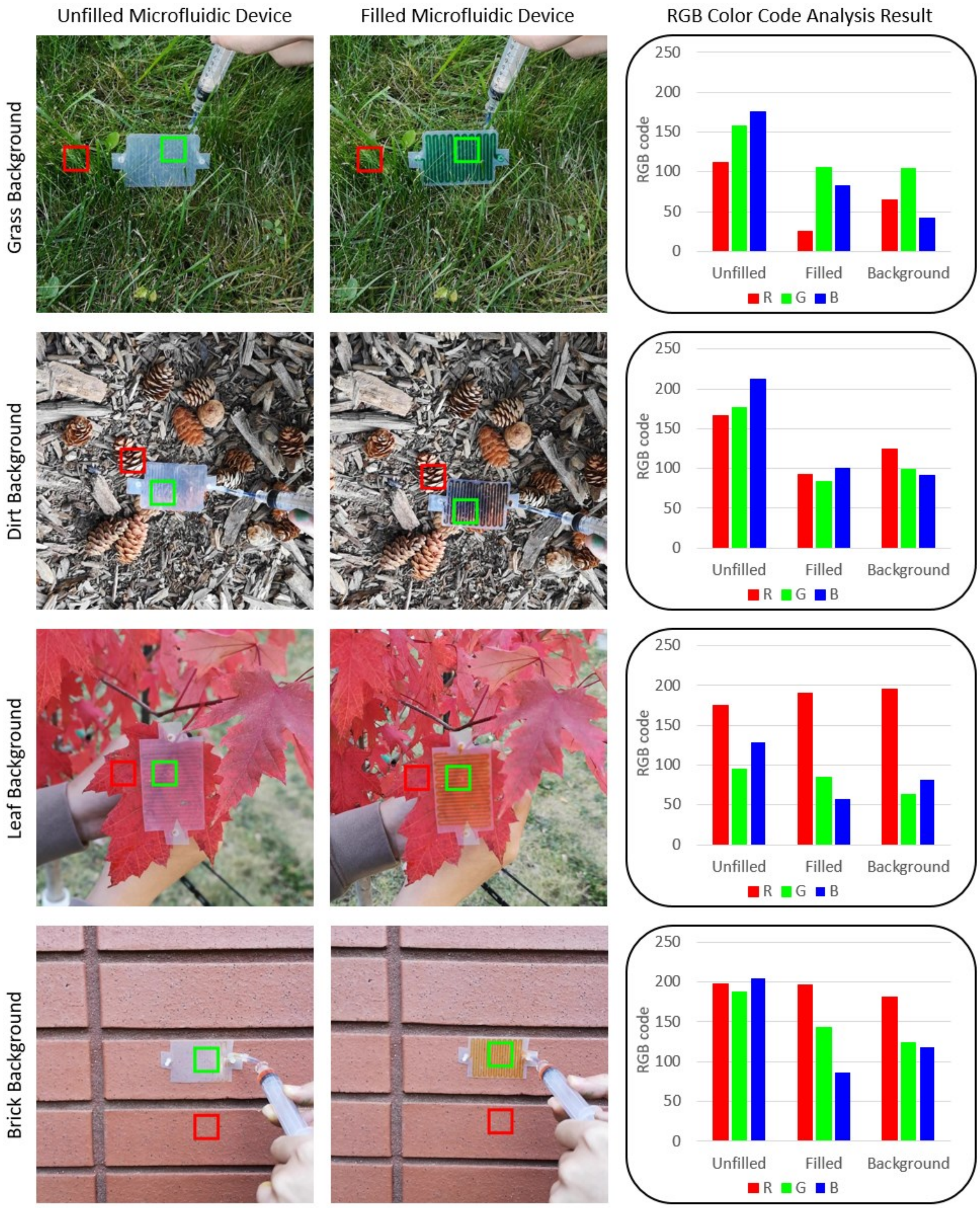

Figure 9. Average color RGB code analysis results for different backgrounds (grass, dirt, leaf, and brick). The first and second columns presented the labeled images to indicate the regions. Red squares are the environmental background regions and green squares are the device regions. The results were presented in the third column, which included all the RGB values for the unfilled device region, filled device region, and background region. The filled device region has very similar RGB values as the background region compared to unfilled device, which indicated the color matching was successful.

IR camouflage is another important application that can be achieved using a modified version of this microfluidic device. In general, smooth surface metals have low emittance but high infrared reflectivity [138], [139]. This makes metal objects thermally visible as long as there is a heat source in the region even the metal object itself does not emit much infrared radiation. The reflection from the heat source makes metal appear to be at a higher temperature. However, this reflected IR radiation can be easily blocked by a thin layer of water. By circulating a layer of water above the reflective metal layer, the IR reflection can be blocked, which makes the metal appear colder (ambient temperature). This allows the manipulation of the IR appearance of metals. Versions of W1, W2, and W3 devices were modified by embedding a metal surface between the channels and the bottom layer. The result of the measurement of their IR appearance was presented in Figure 10.

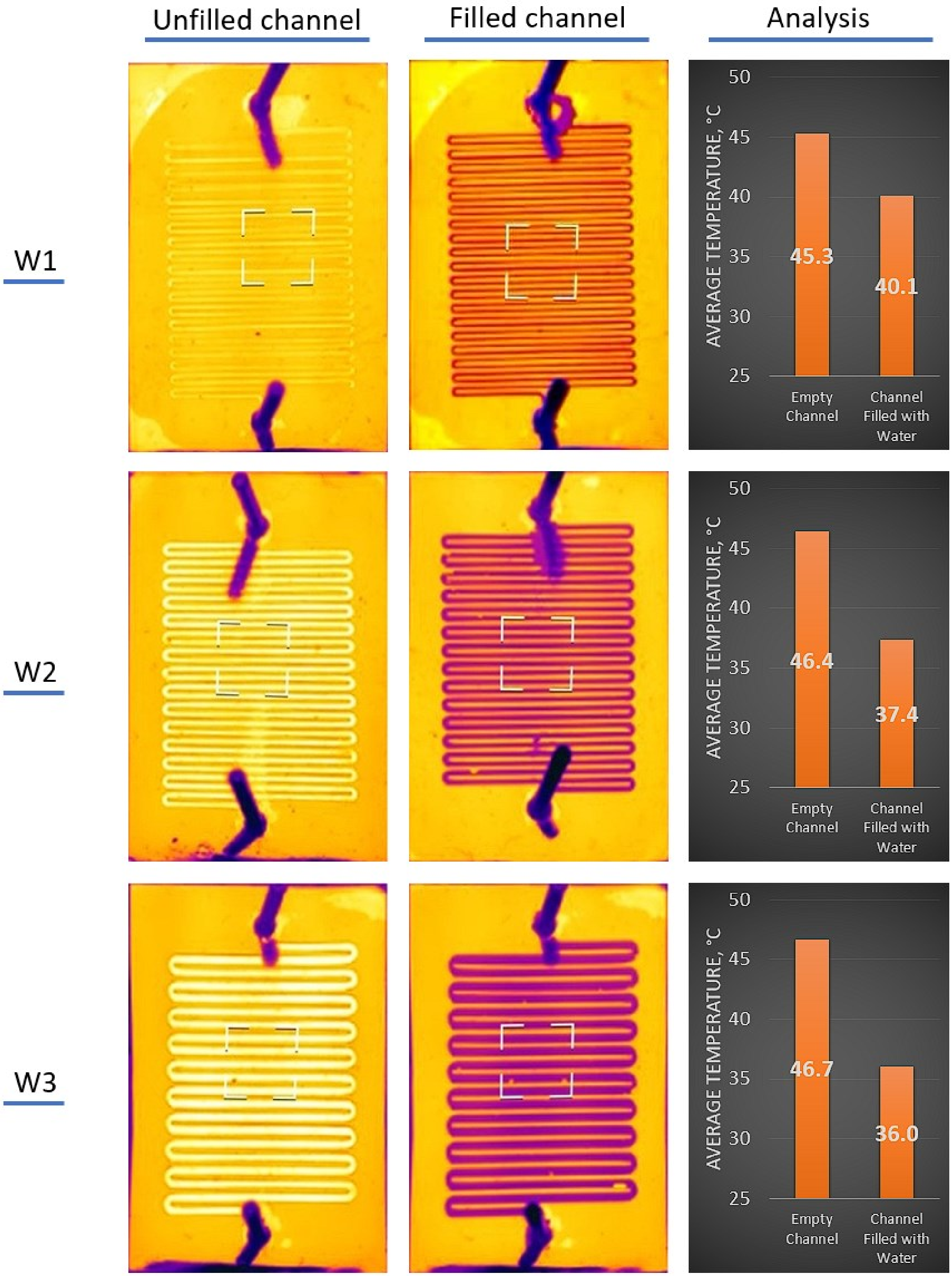
Unfilled channel
Filled channel
Analysis
W1
W2
W3
AVERAGE TEMPERATURE, °C
50
45
40
35
30
25
Empty Channel
Channel Filled with Water
45.3
40.1
46.4
37.4
46.7
36.0

Figure 10. Images of the IR reflection appearance of W1, W2, and W3 positioned in front of a hot 3D printer bed (100℃) under unfilled (column 1) and filled (column 2) states. The average temperature measurement area is indicated in each subfigure in column 1 and column 2 as the white square. Column 3 shows the area average temperature drop upon filling the microfluidic devices with DI water.

The first column in Figure 10 shows the empty channel's IR reflection appearance against a hot 3D printer bed (surface temperature at 100℃); the second column shows the reflection appearance from the filled channel with DI water; and the third column shows the measured average temperatures data of the metal surface by the IR camera for both filled and unfilled channels. The area of measurement was indicated in each subfigures in column 1 and column 2 as a white square. The measured average temperature results for the unfilled W1, W2, and W3 devices were 45.3, 45.4, and 46.7 ℃, respectively. Although the temperature of the heated source was set at 100℃, the highest average reflected temperature was 46.7℃. This could be attributed to the presence of UHMWPE layers above the metal surface. Despite the high IR transparency of the PE sheet, it still absorbed a certain portion of the IR radiation before it reaches the underlaying metal surface. Furthermore, after the IR radiation is reflected from the metal, the PE sheet continued to absorb a fraction of it. As the IR radiation passed twice through the PE sheet before it was detected by the IR camera, it significantly contributed to the observed temperature difference. Another possible factor could be the precision of the IR camera. This type of camera measures the average temperature within a measurement zone rather than the temperature at specific point. Upon filling the devices with DI water, the area average temperatures of W1, W2, and W3 were 40.1, 37.4 and 36.0 ℃, respectively. The area average temperature drop of all devices was 8.3 ℃, demonstrating the effectiveness of our method in blocking reflected IR radiations. Notably, despite the area average temperature drop was lower than 9 ℃, the spot temperature at the channel dropped from 50.1 to 31.6 ℃ upon filling, which was nearly 19 ℃ decrease. Detailed experimental infrared images during the characterization can be found in supplementary information in Figure A6. In addition, the width of the channels had an obvious impact on the reflected IR appearance, with wider channels appearing as colder surfaces. This was primarily due to the large channel area vs. support wall structure that was achieved for these designs and suggests future improvements are possible.

2.4 Conclusion

In this work, we fabricated and characterized microfluidic devices made entirely from polyethylene (UHMWPE) including inlet/outlet tubes (PE). The devices are inexpensive (less than 0.09 CAD per piece), extremely durable, and relatively transparent to both visible light and thermal infrared wavelengths. The fabrication technique is simple and relies solely on xurography and thermal bonding. The fabrication of the microfluidic device is fast (a few minutes per piece), and thanks to the simplicity of the process, it would be possible to mass produce this type of microfluidic device. Our characterization showed the channel was watertight and airtight, which demonstrated the reliability of the device. Besides the unique fabrication process, our group developed some innovative applications of this microfluidic device with microchannels. Due to the transparency of polyethylene, it has been shown that this microfluidic device is capable of achieving visible camouflage by circulating a dyed liquid through the microchannel. A prototype has been fabricated to demonstrate the ability to have multiple camouflage colors on a same device. IR camouflage was achieved by slightly modifying the original structure of the microfluidic device. An ultra thin metalized polyethylene was added between the microchannel layer and the bottom layer. IR reflection tests showed the capability to manipulate the IR reflectivity of metals and therefore the apparent temperature of the system, without altering its actual temperature. Improved thermal infrared performance should be achievable using thinner polyethylene sheets. The low cost, durability, and ease of fabrication of these microfluidic devices, combined with their unique camouflage properties, make them promising candidates for a wide range of applications, including environmental monitoring, medical diagnostics, and military and surveillance operations [1], [2], [114]. The ability to mass produce these devices with minimal resources could lead to significant advancements in these fields and contribute to the development of more accessible and affordable technologies.

Chapter 3

Development of low voltage electrowetting on self-assembled dielectric layers for variable IR appearance

3.1 Introduction

Electrowetting systems and related technologies have been widely researched, fabricated, and developed for over a century from 1875 when Gabriel Lippmann developed the theory of electrocapillarity in his PhD thesis [70], [71], which is the basis of electrowetting [72], [73]. Multiple early-stage works were conducted since then [74]–[81], however, these studies relied upon direct contact at the droplet – electrode interface, which was fundamentally different from modern electrowetting systems, and far from practical applications [73], [76], [79]. The main obstacles of such configuration were the often involvement of toxic heavy metal [82], and the electrolytic decomposition of liquid [72], [79]. Alternative configuration was proposed to solve the decomposition by Berge [73], [83], which implemented a thin layer of insulator film on the electrode to separate the droplet from direct electrical contact. It was known as electrowetting on insulator coated electrodes (EICE), or electrowetting on dielectric (EWOD) [79]. Since then, electrowetting technologies improved rapidly due to the demand of precise manipulations of liquid droplets and the trend of miniaturization. Multiple practical applications were developed [71], [79] including: liquid lenses [84]–[87], electronic displays [88]–[91], and multiple lab-on-a-chip microfluidic assay devices [92]–[94]. More information about the electrowetting developments can be found in other reviews [71]–[73], [76], [79]. However, most of the electrowetting applications are exclusively focused on visible spectrum.

Apart from the narrow application interests range, there are other fundamental challenges in modern electrowetting systems, including a universal phenomenon known as contact angle saturation (CAS), which describes how the contact angle will reach a minimum value at high voltage where the parabolic relationship in Eq(1) fails [72], [96], [99]. Several hypotheses were developed regarding this CAS, however, the mechanism of this phenomenon is still ambiguous

[96], [97], [99], [140]. Early review claimed that no voltage-induced transition from partial to complete wetting has ever been observed [72]. While the first complete wetting was reported in 2013 [141], generic electrowetting system can have a saturation angle as high as 70° - 80° [100]. Besides the contact angle saturation, the high actuation voltage required to achieve large contact angle changes was also a bottleneck for practical applications as most conventional EWOD devices were operating at over 100 V [142], [143]. This was inevitable since the thickness of the dielectric layers was commonly in the range of several hundreds of nanometers to tens of micrometers [142], [144], Even with such high voltage, the contact angle decreases were often just dozens of degrees due to CAS [99]. Moreover, the manufacturing of such dielectric layers used complicated processes such as electron beam deposition, sputtering [145], plasma-enhanced chemical vapor deposition [146], and spinning coating [142], [147], [148]. Several innovative works were performed to mitigate the challenges by introducing an alternative configuration, including a self-formed lipid bilayer as main dielectric layer [144], [149], [150]. The actuation voltage in these systems was extremely low (several volts or even without external voltage) owing to the thickness of the bilayer being only several nanometers [149], [151]. However, there were still some remaining drawbacks such as the usage of a liquid metal EGaIn, which is expensive and whose geometry is hard to control [152]. Other approach also involved the usage of rare earth metal hafnium which has the abundance of only 4.5ppm in the earth's crust [153].

Besides the visible spectrum, there is great potential in applications within the infrared spectrum, such as IR camouflage, a highly sought-after topic [113]. Multiple IR camouflage approaches has been reported by using nanostructured polymers that alternate reflection, using thin film to control emission and manipulating diffraction, applying smart textiles, and micro-scale designed metamaterial to tune emissivity [114], [117]–[121]. Our group has recently reported an adaptive visible and IR camouflage control system based on thermally transparent pressure-driven microfluidics [39]. However, as the scaling law indicates: $\Delta p/L \propto l^{-4}$which means the pressure drop rate is to the fourth power of the scale reduction ratio. It becomes difficult to drive liquids through microfluidic channels using pressure [154]. Also, the actuation time is relatively long since the water has to travel along the channel to achieve adaptive camouflage. Therefore, We aimed to develop a fast-actuated, innovative IR camouflage system without pressure-driven flows.

In this study, we developed a low voltage (~3.4V DC) fast actuated, nearly complete wetting (~15° of wetting contact angle), inexpensive (less than 1 Canadian dollar per setup), simple-to-manufacture configuration for an electrowetting on dielectric system. No dielectric layer deposition process or clean-room facility is required. Our system uses a metalized (aluminum coated) polyester film commonly found in emergency blankets and reflective insulation as the electrode; an aluminum oxide layer spontaneously formed on top of the film, which ensured stability [155]. The system was submerged in dodecane with sorbitan trioleate surfactant, while the droplet was made of distilled water containing another surfactant - sodium dodecyl sulfate (SDS). This configuration decreased the σ_{lv} significantly due to the inclusion of surfactants. Furthermore, an ultra-thin lipid bilayer will form upon the application of a water droplet in dodecane acting as a dielectric layer [149], [156].

More importantly, inspired from the optical display applications of the electrowetting system, we conceived another innovative direction for electrowetting – the high IR transmittance nature of dodecane [157], which allows this system to achieve adaptive IR camouflage by manipulating the reflected IR appearance of the metalized polyester electrode via an electrowetting droplet on top of it. Several modifications were applied towards the goal of IR. Multiple characterization results indicated that this electrowetting system has the capability to achieve adaptive infrared camouflage.

3.2 Experimental Methodology

3.2.1 Theoretical Model

The electrowetting behaviour can be modeled using the Lippmann – Young's equation, which predicts the change in contact angle upon the application of an external voltage across the interface [72]

$$\cos\theta(U) = \cos\theta_{\mathrm{Y}} + \frac{\varepsilon_0\varepsilon_1}{2d_{\mathrm{H}}\sigma_{\mathrm{lv}}}\left(U - U_{\mathrm{pzc}}\right)^2 \tag{1}$$

where θ is the contact angle of the liquid droplet, θ_{Y} is the Young's angle (*i.e.*, the equilibrium angle when no voltage applied), ε_0 is the vacuum permittivity ($\approx 8.854\cdot 10^{-12}$ F·m^{-1}), ε_1 is the dielectric constant of the liquid, d_{H} is the thickness of the dielectric layer, σ_{lv} is the interfacial tension between the liquid droplet and vapour (note that the ambient phase was denoted as "vapour" for simplicity, but it can be another liquid immiscible with the droplet), U is the applied voltage, and U_{pzc} is the potential zero charge, which represents the voltage required to compensate for the spontaneous charging of the electrode.

By combining the terms for capacitance $C = \frac{\varepsilon_0\varepsilon_1}{d_{\mathrm{H}}}$ and using the assumption that the surface of the insulating layer does not give rise to spontaneous absorption of charge (*i.e.*, the U_{pzc} was set as zero), Eq(1) can be rewritten as:

$$\cos\theta(U) = \cos\theta_{\mathrm{Y}} + \frac{CU^2}{2\sigma_{\mathrm{lv}}} \tag{2}$$

where C is the capacitance per unit area of the dielectric layer.

3.2.2 Materials

Metalized polyester (0.002" thick Mylar Film with surface coated with aluminum, Amazon), and copper foil tape (dual conductivity adhesive tape, ELK) were utilized as the electrode for the electrowetting system and connection to the external voltage. Laboratory grade dodecane (Sigma Aldrich) was used as the ambient phase. A non-ionic surfactant, sorbitan trioleate, was added to dodecane in order to decrease the actuation voltage. Distilled water was used as the actuating liquid drop. Another surfactant, sodium dodecyl sulfate, was added to the water for the same purpose of reducing the activation voltage by lowering the surface tension. Ultra-high molecular weight polyethylene (UHMWPE, thickness = 0.01", McMaster Carr) was used to limit the droplet to a confined area. Water soluble pigmentation was used to dye the water droplet for easier observation during experiments. A thin stainless-steel wire was used as electrode. All the materials were used without modifications and can be considered commercial off-the-shelf (COTS) components.

The concentration of the sorbitan trioleate in dodecane was 0.8 wt%, and the sodium dodecyl sulfate in the distilled water droplet was 3 wt%. Some particular conditions should be noticed in order to form a stable lipid bilayer. The concentration of surfactant (sorbitan trioleate in our study) must be over 0.1 wt%, and the water droplet must be applied onto the electrode after it is submerged in the dodecane. More information can be found in this study [149].

3.2.3 Equipment

A digital tensiometer setup (Smartphone-based tensiometer, Droplet Lab Instrument, Canada) was used for accurate measurement and monitoring of the droplet. The droplet images were captured by the embedded smartphone while the droplet was applied by the default threaded plunger syringe. A 3D printer (Ender 3, Creality 3D, China) heating bed was used as a thermal source for the infrared reflection characterization. A Thermal Imaging Camera (E75, Teledyne FLIR LLC, US) was used for thermal characterizations of reflected heat. A direct current power supply (LWK605D, LONGWEI, China) was used for external voltage application across the electrode and droplet. An analytical electronic balance (ZQ-563, BAOSHISHAN, China) was used to assist the configuration and characterization operations. A digital camera (iPhone 13 Pro Max, US) was used to capture the visible appearance of the droplet wetting behaviour. A flat glass petri dish was used as a container for the dodecane-based ambient phase. A digital multimeter (U1252B, Agilent Technologies, US) was used to measure the capacitance across the system. A schematic diagram of the initial system is shown in Figure 11.

3.2.4 Preparation and Modification

Four configurations were prepared to measure and observe the change in contact angle, the change in visible appearance, the change in IR appearance, and demonstrated the capability to control the wetting direction.

3.2.4.1 Preparation of Configuration 1

Configuration 1 was prepared for the observation of contact angle. The metalized polyester was cut to a 30mm*30mm square piece and taped on the bottom of a petri dish with the metal side facing up. The metal side was connected to the power supply by adhering the copper tape directly on the metalized polyester. The contact angle measurement system used a vertical stainless steel needle filled with distilled water and surfactant. The needle was connected to the power supply with a piece of copper tape connected to alligator clips. The petri dish was filled with dodecane-surfactant liquid until the needle tip was submerged and the needle was then lowered until it was close to the metal surface. Finally, a droplet of water/surfactant was dispensed and kept in contact with both the needle and the metal side. A small voltage across the electrodes could then be applied to activate droplet electrowetting. A schematic setup is demonstrated in Figure 11a.

3.2.4.2 Preparation of Configuration 2

Configuration 2 was modified for the observation of visible appearance change. The vertical needle in the configuration 1 blocked the view from top and resulted in a distorting top view image. Such concerns were mitigated by replacing the needle with a thin steel wire to make the contact with the droplet. The thin wire was connected directly to the power supply clamped by alligator clips, the rest of the system remained the same.

3.2.4.3 Preparation of Configuration 3

Configuration 3 was prepared for the observation of IR appearance. Due to the nature of dodecane of high viscosity [158], it tended to cling on the wire due to capillary action and form a curved region surrounding the wire. Such region created an IR distortion due to the curvature of dodecane surface. Therefore, configuration 3 included planar electrodes so that the distortion was eliminated. Two pieces of metalized polyester was cut into the size of 15mm*30mm as electrodes. The planar electrodes were taped to the bottom of the petri dish, similarly to what was done previously in configuration 1, The electrodes were taped next to each other without forming an electrical contact. The droplet was discharged between the electrodes and the power supply was connected to both electrodes to provide voltage across the system. The biggest advantage of such setup was eliminating the vertical electrode to provide an undistorted top view. A schematic setup is demonstrated in Figure 11c.

3.2.4.4 Preparation of Configuration 4

Configuration 4 was prepared to demonstrate the controllability of the droplet. Two extra UHMWPE pieces were cut into the size of 10mm*30mm and added to configuration 3 as boundaries to create a semi-confined region for it. With the boundary, the droplet can be actuated primarily in one dimension. A schematic setup is demonstrated in Figure 11d.

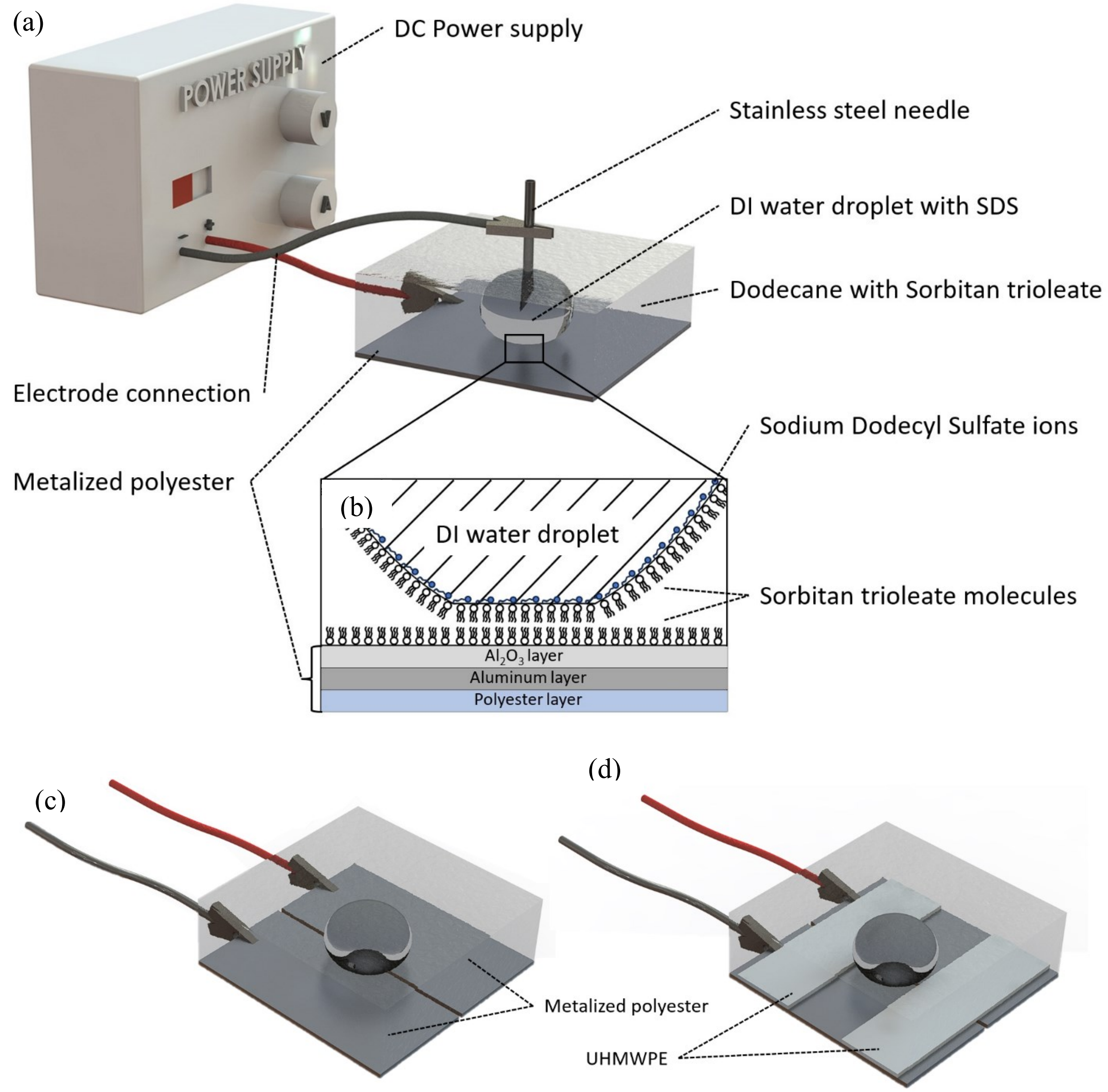

Figure 11. (a) Schematic representation of the configuration 1 electrowetting system that has been developed in this work. The power supply in this system offers direct current external voltage, the negative pole was connected to a deionized water droplet via a stainless steel syringe tip. The positive pole was connected to the metalized polyester via a copper tape. The droplet contained 3 wt% of SDS (sodium dodecyl sulfate) that was submerged in dodecane with 0.8 wt% of sorbitan trioleate. The presented condition is unwetted (no electric voltage applied across the system). (b) A close-up view at the droplet-oil-electrode interface to demonstrate the lipid bilayer composed of sorbitan trioleate spontaneously formed between the interfaces. SDS surfactant ions remain in the water droplet congregate on the interface between the water and dodecane which does not influence the lipid bilayer since SDS ions are mainly inside the water droplet [159]. The aluminum oxide layer was also spontaneously formed on top of the metalized polyester due to oxidation. Note that the thicknesses of these layers, sizes of surfactant molecules and ions, and the droplets are not to scale. Several research also suggest similar structures [144], [149], [159]. (c)

Schematic representation of configuration 3 which replaced the vertical electrode by two planar electrodes providing a non-distorted top view, the droplet was placed in the middle of the electrodes and the power supply was directly connected as demonstrated. The droplets can be actuated in an un-controlled area. (d) Schematic representation of configuration 4 which added two pieces of UHMWPE as boundaries. The rest of the setup remained the same as configuration 3, however, the boundary creates a semi-confined region for water so the droplet can be actuated mainly in one direction.

3.2.5 Characterization

3.2.5.1 DC Electrowetting Performances and Characteristics

The electrowetting performance was characterized based on configuration 1. The lipid bilayer thickness was estimated from the measurement of the capacitance of it according to the following equation:

$$C = \frac{\varepsilon_0 \varepsilon_1 * A}{D} \tag{3}$$

where C is the capacitance for parallel plates, A is the area of this capacitor, and D is the distance between the parallel plates, ε_0 is the vacuum permittivity ($\approx 8.854 * 10^{-12} \mathrm{F} \cdot \mathrm{m}^{-1}$), and ε_1 is the dielectric constant of the material. Since the lipid bilayer's thickness is in the range of nanometers [151] due to the nature of oleate molecular length and could not be directly measured due to the resolution of optical microscope (the diffraction limit is at 200-300 nm [160]). The contact angle change upon wetting was determined using the digital tensiometer. Detailed calculations are provided in the results section.

3.2.5.2 Electrowetting System Visible Appearance Characteristics

In order to improve the visibility of the droplet on the metalized surface, the water droplet was colored using water soluble pigments for the visible appearance characterization. Configuration 2 was used to provide a better top view of the system. By gently touching the droplet with the wire and applying the voltage across the electrodes, the droplet can be actuated. One thing to note is that avoiding direct contact between the wire and the planar electrode is necessary to prevent short circuiting the whole system. The visual images were captured by digital cameras to demonstrate the coverage area change.

3.2.5.3 Electrowetting System IR Camouflage Performances and Characteristics

The electrowetting system IR camouflage tests were performed using configuration 3 with the IR camera pointed at 45° to observe the electrode and droplet that was reflecting the IR radiation from the heat source (3D printer heating bed @ 383 K). The IR images before and after electrowetting actuation were captured for a measurement of the coverage area. The configuration 4 was also tested to demonstrate the controllability of the droplet which can be more accurate when wetted in a preferential direction. Figure 12 shows the schematic of the testing scenarios for both the unwetted state (Figure 12a) and wetted state (Figure 12b). As shown in Figure 12, the radiation from the heat source underwent absorption, transmission, and reflection by the electrode. It is worth noting that even though dodecane has a high infrared transmission at these wavelengths (allowing IR to pass through), a thick layer of dodecane will absorb most of the IR radiation (which passes through the layer twice in this reflection mode), which is undesirable. Therefore, we also performed an experiment to seek the effect of the thickness of dodecane on the observed temperature. The dodecane thickness-observed temperature relationship was characterized by gradually removing dodecane from the petri dish while observing the apparent temperature from the electrode using configuration 1 but without the needle. The thickness of the dodecane was estimated based on the weight added to the dish and the area of the dish.

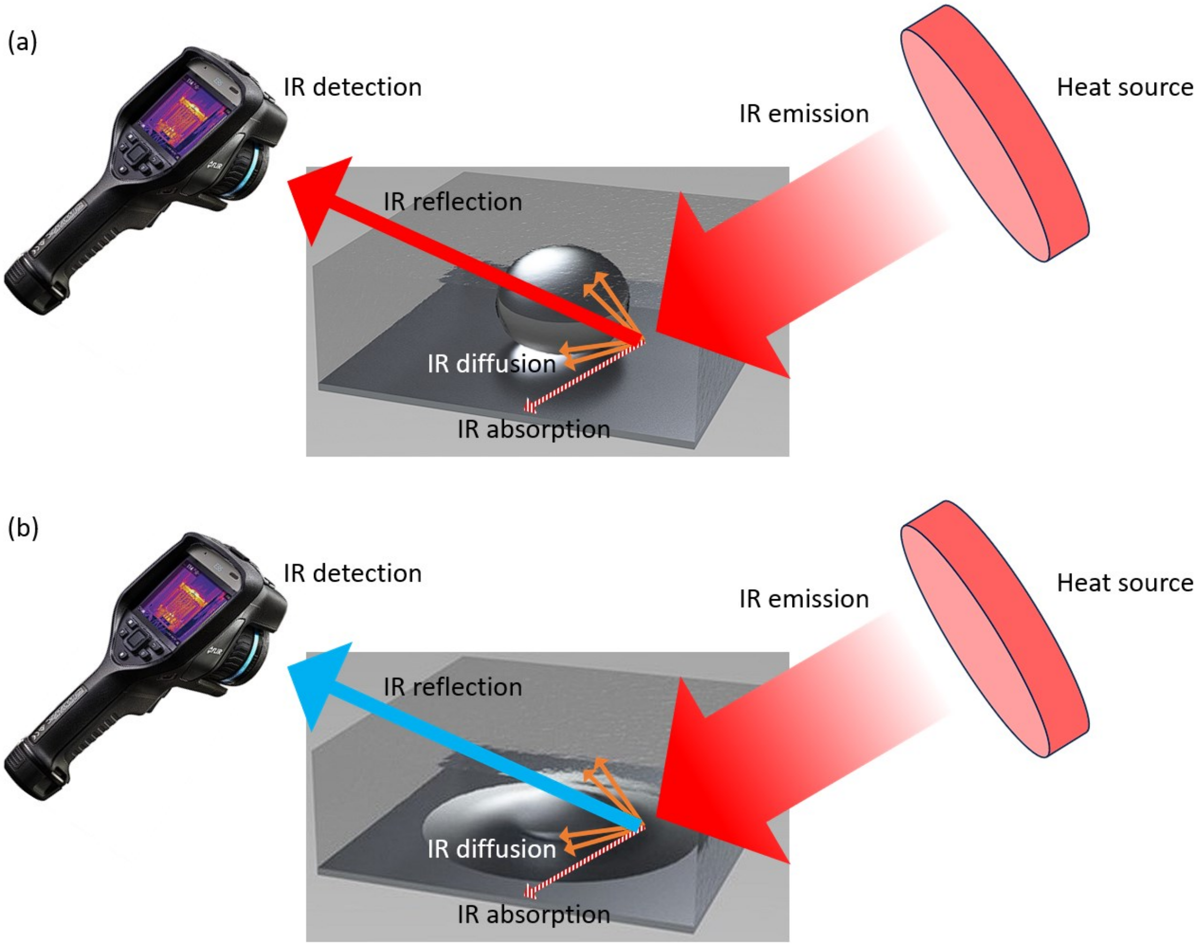

Figure 12. Schematic representation of the IR camouflage testing setup for the electrowetting system. (a) and (b) show two different states of system (wetted and unwetted) and their thermal detection mechanism where the 3D printer bed acted as heat source and emitted IR radiation, which was reflected by the electrode and finally observed by an IR camera. Since water has very low IR transmittance (IR opaque), the wetted droplet will block the reflected radiation from the electrode and resulted in the decrease of observed temperature.

3.3 Results and Discussion

The contact angles of the droplet for both a wetted and unwetted state were demonstrated in Figure 13. The droplet remained hydrophobic with a contact angle of 133° when no external voltage applied. When the droplet was actuated by only 3.6V DC, it achieved nearly complete wetting with a contact angle of 15°. This voltage of 3.6 V DC is much lower than what is observed in conventional electrowetting systems.

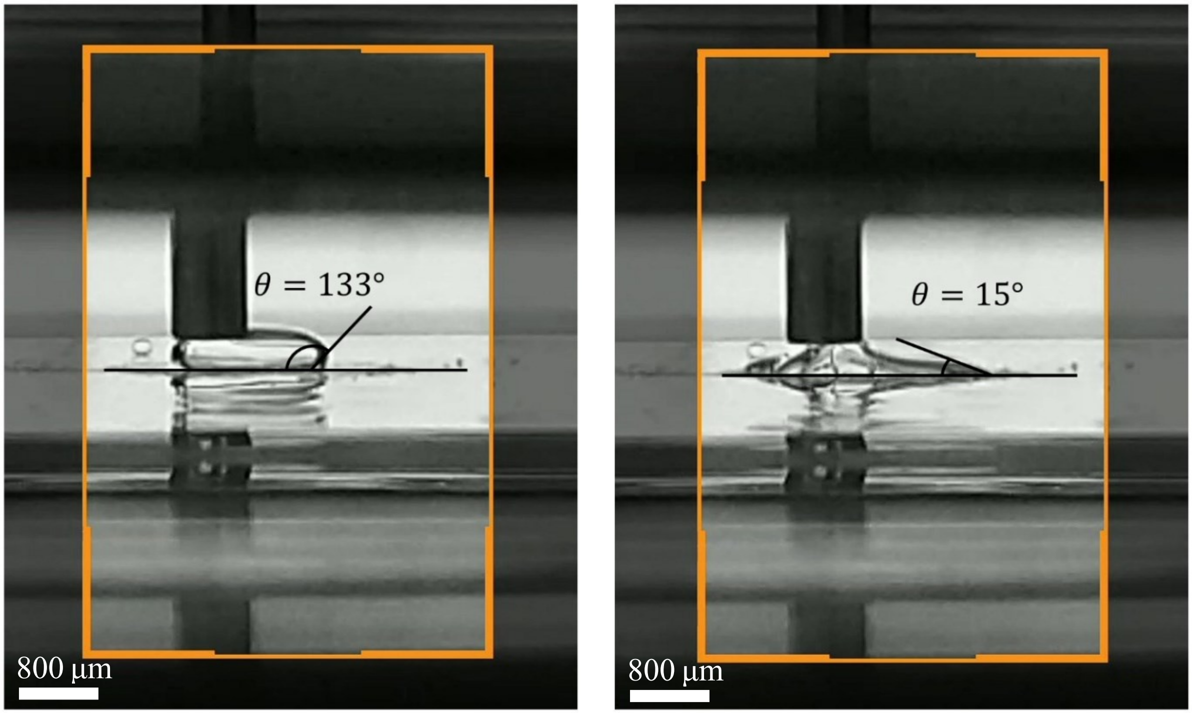

Figure 13. Images of the droplet which achieved complete wetting actuated by 3.6 V DC. The contact angle changed from 133° to 15° by applying voltage across the droplet and electrode (metalized polyester). (a) demonstrated the unwetted state with no external voltage applied, (b) demonstrated the wetted state with 3.6V applied. The wetting process is fully repeatable.

One of the main reasons for this low actuation voltage was that the lipid bilayer that spontaneously formed at the interface acted as a dielectric layer, which were basically made of two layers of sorbitan trioleate molecules. It draws our attention that the lipid bilayer must have a thickness in the range of nanometers to decrease the voltage from several hundred volts to several volts. According to Eq(1), the relationship between applied voltage and dielectric layer thickness follows $U^2 \propto d_{\mathrm{H}}$ for the same contact angle change. Therefore, reducing the dielectric thickness by a factor of 100 can only result in a reduction of the required voltage by a factor of 10. A characterization was developed to measure the thickness of sorbitan trioleate lipid bilayer. Since the contact interface was smooth and flat, it can be assumed as two capacitors made of lipid bilayer and aluminum oxide respectively connected in series. The visualization of the capacitor circuit was shown in Figure 14. Although it seems possible to calculate the capacitance of aluminum oxide, owing to it being a naturally formed oxidation layer, the thickness of aluminum oxide cannot be certain, therefore, an alternative approach was developed. The overall capacitance measured across the circuit is 0.042 nF, and the capacitance of the aluminum oxide is 0.043 nF. The capacitance of the lipid bilayer can be calculated based on these as 1.806 nF. The area of lipid bilayer was estimated by assuming the contact region is a circle with the diameter same to the needle (0.80 mm). According to Eq(3), the thickness of lipid bilayer was calculated as 4.928 nm. This quantity validated the hypothesis that low actuation voltage is possible when the dielectric layer is thin enough. This value is also very close to double the carbon chain length of the oleate molecule [151].

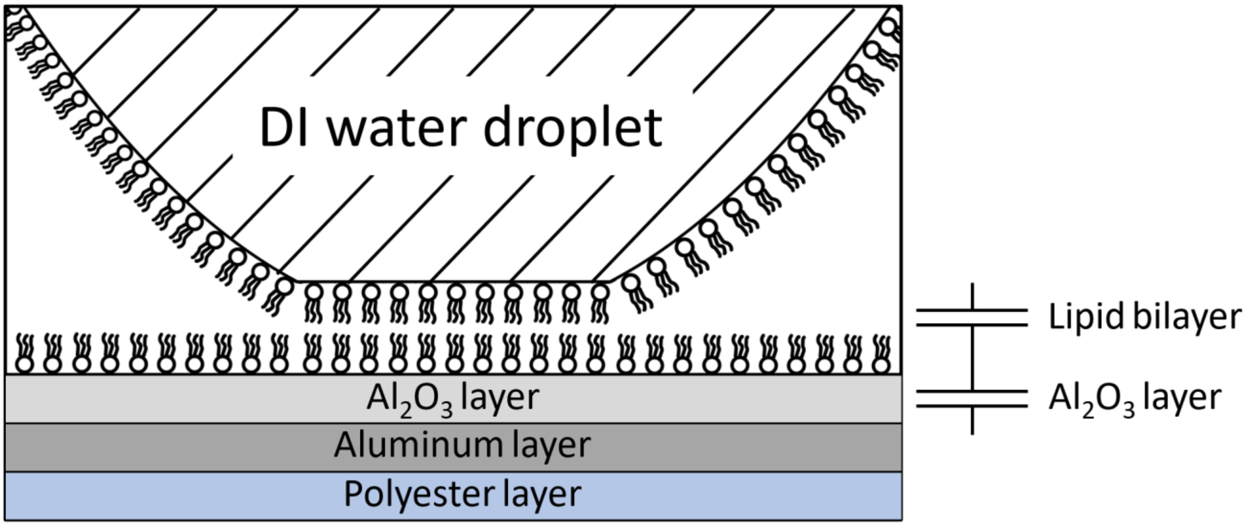

Figure 14. A detailed-look of the interface between the droplet and electrode. The SDS surfactant in water droplet is neglected since it does not involve in the formation of lipid bilayer. The lipid bilayer can be simplified as a parallel plate capacitor connected in series to another parallel plate capacitor made of aluminum oxide.

It is worth noting that obvious change in apparent temperature only appeared when the dodecane layer is very thin as dodecane also absorbs the portions of the IR radiation wavelengths. Therefore, we characterized the relationship between the thickness of dodecane and apparent temperature from the reflection of electrode. The heat source was set at 333 K for safety reasons. We noticed that the apparent temperature changed significantly along with the thickness of dodecane. Therefore, the dodecane was removed gradually from the system, the weight of dodecane and the apparent temperatures were recorded respectively, and the thickness of dodecane was then estimated by the weighing method. The result was presented in Figure 15, which revealed an interesting trend of changing, the appeared temperature almost stayed constant (close to room temperature 296 K) when the thickness was decreased from over 4000 μm to around 1100 μm. After this point, the apparent temperature increased rapidly with only small amount of decrease of dodecane thickness and appeared closer to the heat source (333 K). The shape of the curve is very likely an exponential curve, as the intensity of the light in water versus the depth has an exponential relationship [161]. However, the relationships between the appeared temperature and the thickness of dodecane is still under investigation. With the relationship being revealed, later IR appearance tests were performed with preferable thickness of dodecane to demonstrate significant temperature change upon electrowetting.

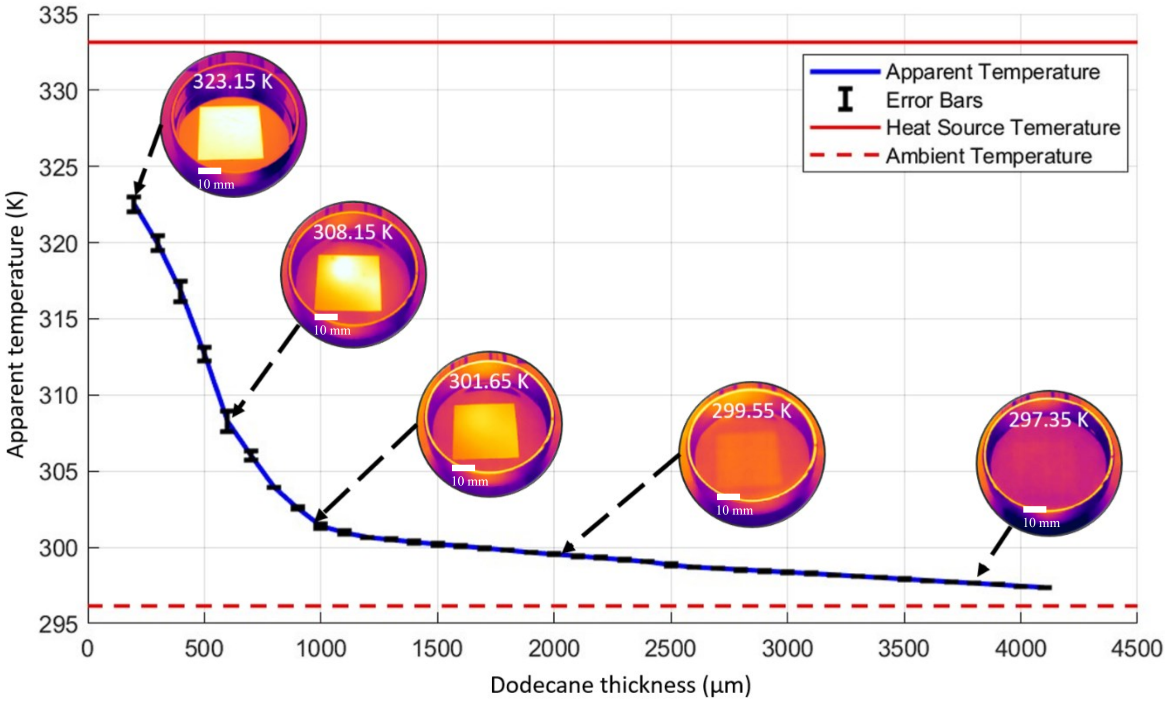

Figure 15. The computer generated averaged line of appeared temperature versus dodecane thickness. This line included three separated completed measurements of the system. The error bars are also included in the graph, since the temperature changed rapidly when the dodecane thickness fell bellow 1100 µm, the measurements shared an increase of human measurement error. The errors were mainly due to the precise removal of dodecane. The curve shape is highly similar to an exponential curve. Several representative IR camera measurement images are also presented to show different apparent temperatures with different thickness of dodecane. The apparent temperatures are indicated on the curve respectively. Ambient temperature (296 K) and heat source temperature (333 K) are indicated on the plot.

Figure 16 presents the infrared images of the electrowetting system. Smooth metalized surface like the electrode used in this electrowetting system typically have high IR reflectivity [138], [162], it makes such materials highly detectable though IR camera especially when there are heat source nearby. The reflected heat source's IR radiation from the metal surface will appear very distinct in comparison to the surrounding non-reflective material. Fortunately, reflected IR radiation can be eliminated by just a thin layer of water since water has low IR transmittance [163]. By wetting the droplet on the metal electrode, the apparent temperature dropped significantly from around 323 K to a near ambient temperature of 298 K. The apparent temperature change is demonstrated in Figure 16 where the water droplet appears much colder than surrounding. In addition to the temperature difference, the electrowetting behaviour was evident under the IR camera with the coverage of the droplet increasing over 50% upon wetting. The unwet droplet had an area of 17.09 mm^2 while the wetted droplet was 25.86 mm^2 (151.3% larger). The length of droplet increasing over 50% in the controlled planar electrode configuration. The unwet droplet had the longest vertical length of 6.08 mm while the wetted droplet was 9.33 mm (153.4% longer). Figure 16 also shows the visible electrowetting from vertical direction in the steel wire configuration with a dyed water droplet. Furthermore, the average wetting actuation time was about one second (1.00 ± 0.33 s). Overall, the electrowetting system shows the capability to achieve IR camouflage with multiple vital features: the wetting of droplet can reversibly alter the IR appearance, the system actuation time is short (few seconds), and the actuation voltage is very low (3.6 V).

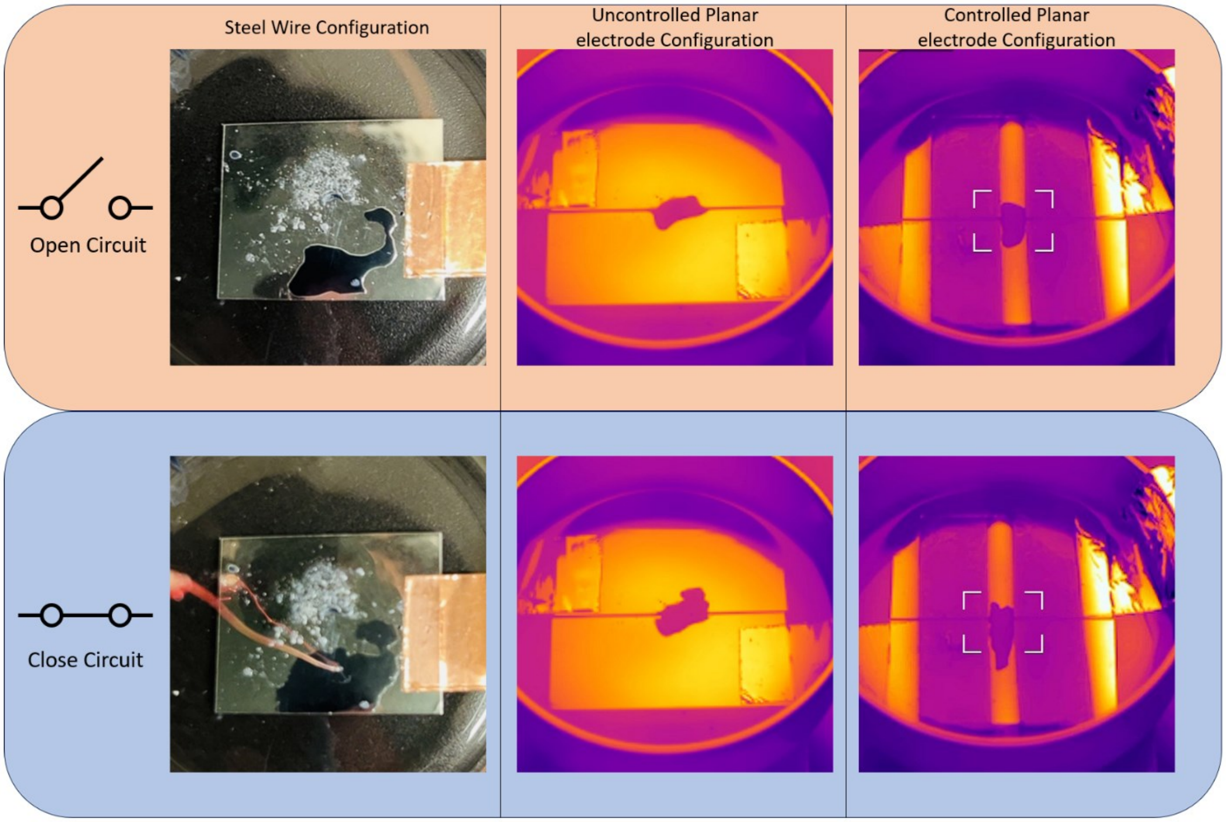

Figure 16. The first column demonstrated the visual appearance of the electrowetting system as the steel wire configuration, the black droplet was pigmented water to improve the visibility. By touching the droplet

with the voltage-applied wire, the droplet had nearly complete electrowetting and the coverage area increased dramatically upon wetting. Images of the IR reflection appearance of the droplet in the electrowetting system positioned beneath a heated 3D printer bed with the temperature set as 383 K. The electrowetting system's IR appearances were presented in column 2 & 3. The second column presented the uncontrolled planar electrode configuration, in the IR image, the two planar electrodes were very obvious (arranged up and down) as the electrodes appeared hotter than the ambient due to the reflection of IR radiation. The droplet appeared as ambient temperature and the coverage area increased over 50% compared to unwetted droplet within a few seconds upon wetting. The third column presented the controlled planar electrode configuration by simply adding UHMWPE boundaries to confine the droplet in one dimensional movement. It indicated an obvious increase of coverage area as the length of the droplet increased significantly due to wetting. These demonstrated the thermal appearance manipulation can be achieved by presented electrowetting configurations.

3.4 Conclusion

In this study, we demonstrated an innovative electrowetting-on-dielectric system that has the key features of low actuation voltage, nearly complete wetting, inexpensive, simple to manufacture with all commercial off-the-shelf (COTS) components. More importantly, we demonstrated this electrowetting system has the capability to achieve adaptive infrared camouflage. The system utilized surfactants to decrease the interfacial tension dramatically and an ultra thin lipid bilayer is spontaneously formed and acted as a dielectric layer. Also, the system received multiple modifications of configuration to improve the controllability of the droplet. Our characterizations demonstrated a strong potential in the field of IR camouflage owing to the low actuation voltage, high temperature change, and fast actuation time. The appeared temperature-dodecane thickness relation was also investigated along with the IR camouflage characterization. Overall, this electrowetting system presented multiple unique features comparing to the conventional system, which could lead to more innovative development in these fields and further work to encapsulate pixels for IR switching for future development.

Chapter 4

Concluding remarks and future directions of research

4.1 Conclusion

In this thesis research, we aimed to develop and characterize devices that are capable of achieving adaptive visible and infrared camouflage control while being low-cost, energy efficient, short fabrication time, robust and reconfigurable.

In the **initial phase** of this research work, as presented in Chapter 2, we developed and characterized innovative microfluidic devices made entirely from polyethylene including inlet/outlet tubes with a novel interface between the device and tubing. The devices are low-cost (less than $0.09 CAD per piece) and extremely durable due to the nature of UHMWPE. The fabrication technique is simple and relies solely on xurography and thermal bonding, which is fast (a few minutes per piece) and the reconfiguration can be achieved by designing new xurography pattern and using different thicknesses of polyethylene sheet. UHMWPE was selected as the main material of the device because it remains mechanically stable above its melting point, preserving the channel features during thermal bonding. This microfluidic device is capable of achieving visible camouflage by circulating a dyed liquid through the microchannel. A prototype has been fabricated to demonstrate the ability to have multiple camouflage colors on a same device. IR camouflage was achieved by slightly modifying the original structure of the microfluidic device with an ultra thin metalized polyethylene layer, enabling liquid circulation over the metal to modify its reflected IR appearance. IR reflection characterization showed the capability to manipulate the IR reflectivity of metals and therefore the apparent temperature of the system, without altering its actual temperature. Overall, the low cost, durability, and ease of fabrication and reconfiguration of these microfluidic devices, combined with their unique camouflage properties, make them promising candidates for a wide range of applications, including environmental monitoring, medical diagnostics, and military and surveillance operations.

In the **second phase** of this research work, as presented in Chapter 3, we aimed to develop and characterize another electrowetting device and determine if it could achieve infrared camouflage control by manipulating a droplet on metal surfaces. In this phase, all the design choices were made towards the IR appearance control. Dodecane was selected as the submerging oil interface because it is infrared transparency, and DI water was used as the droplet on the electrode. The contact angle measurement tool's needle was replaced by a planar electrode to avoid creating disturbing top view IR images. The relationship between the thickness of dodecane and the apparent reflected temperature from electrode was also characterized, although dodecane is IR transparent, it still absorbs IR radiation. Therefore, a thinner layer of dodecane is preferred. By using surfactants in both water (with 3w% SDS) and dodecane (with 0.8w% of sorbitan trioleate), the contact angle was significantly reduced which resulted in an increased coverage area. We also overcame one of the biggest challenges - contact angle saturation - with only 3.6 V DC. This electrowetting system presented multiple unique features compared to the conventional system, suggesting potential for innovative development in these fields. Overall, we demonstrated an innovative electrowetting-on-dielectric system with low actuation voltage, nearly complete wetting, inexpensive setup, simple fabrication processes with all COTS components. Multiple characterization results indicated this electrowetting device has the capability to achieve adaptive infrared camouflage.

4.2 Possible Future Directions

Based on accomplished works, the following future directions of research are identified:

- Investigation into the polarity limitation observed during the electrowetting device experiment, where the original configuration was used. This configuration involved a stainless-steel needle and an aluminum-coated, metalized polyester as the electrode. With this combination, the system could only be actuated when the negative pole was connected to the stainless-steel needle and the positive pole to the aluminum electrode. The water droplet appeared to decompose when the poles were flipped. The electrochemical mechanism underlying this phenomenon has not yet been fully understood and requires further future experiments and characterizations.

- Investigation into strange donut shape water droplet formed on metalized polyester submerged under dodecane oil. Interestingly, the formation seems to occur spontaneously without external power input. This phenomenon was first observed during regular electrowetting testing. The droplet contained 3 wt% of SDS (sodium dodecyl sulfate) and was submerged in dodecane with 0.8 wt% of sorbitan trioleate. We observed that the water droplet transforms into a donut shape, with the ring getting thinner until it eventually breaks, returning to a spherical shape. This entire process occurs without any external voltage. The mechanism behind this is still unknown and requires future work but means that complete understanding of all aspects of the electrowetting process is a priority to make this system viable for thermal appearance switching.
- Integration of electrowetting with thermally drawn hollow fibers that have an internal metal layer. Our group is currently exploring thermally drawn smart fibers. At present, the filling of thin fibers relies on pressure-driven flow of liquid. However, due to fluidic resistance to flow in ultra small channels, it can be challenging to fill the fiber quickly. It may be possible to incorporate electrowetting, so that water can autonomously "climb" inside the fiber with a minimal voltage input and scaling laws become favorable for that type of fluid control in microchannels.

References

[1] G. M. Whitesides, "The origins and the future of microfluidics," *Nature*, vol. 442, no. 7101, Art. no. 7101, Jul. 2006, doi: 10.1038/nature05058.

[2] K. Ren, J. Zhou, and H. Wu, "Materials for Microfluidic Chip Fabrication," *Acc. Chem. Res.*, vol. 46, no. 11, pp. 2396–2406, Nov. 2013, doi: 10.1021/ar300314s.

[3] A.-G. Niculescu, C. Chircov, A. C. Bîrcă, and A. M. Grumezescu, "Fabrication and Applications of Microfluidic Devices: A Review," *Int. J. Mol. Sci.*, vol. 22, no. 4, Art. no. 4, Jan. 2021, doi: 10.3390/ijms22042011.

[4] P. Gravesen, J. Branebjerg, and O. S. Jensen, "Microfluidics-a review," *J. Micromechanics Microengineering*, vol. 3, no. 4, p. 168, Dec. 1993, doi: 10.1088/0960-1317/3/4/002.

[5] D. Erickson and D. Li, "Integrated microfluidic devices," *Anal. Chim. Acta*, vol. 507, no. 1, pp. 11–26, Apr. 2004, doi: 10.1016/j.aca.2003.09.019.

[6] S. C. Terry, J. H. Jerman, and J. B. Angell, "A gas chromatographic air analyzer fabricated on a silicon wafer," *IEEE Trans. Electron Devices*, vol. 26, no. 12, pp. 1880–1886, Dec. 1979, doi: 10.1109/T-ED.1979.19791.

[7] K. E. Petersen, "Fabrication of an integrated, planar silicon ink-jet structure," *IEEE Trans. Electron Devices*, vol. 26, no. 12, pp. 1918–1920, Dec. 1979, doi: 10.1109/T-ED.1979.19796.

[8] F. C. M. Van De Pol and J. Branebjerg, "Micro Liquid-Handling Devices - A Review," in *Micro System Technologies 90*, H. Reichl, Ed., Berlin, Heidelberg: Springer Berlin Heidelberg, 1990, pp. 799–805. doi: 10.1007/978-3-642-45678-7_115.

[9] A. Manz, N. Graber, and H. M. Widmer, "Miniaturized total chemical analysis systems: A novel concept for chemical sensing," *Sens. Actuators B Chem.*, vol. 1, no. 1, pp. 244–248, Jan. 1990, doi: 10.1016/0925-4005(90)80209-I.

[10] J. Hwang, Y. H. Cho, M. S. Park, and B. H. Kim, "Microchannel Fabrication on Glass Materials for Microfluidic Devices," *Int. J. Precis. Eng. Manuf.*, vol. 20, no. 3, pp. 479–495, Mar. 2019, doi: 10.1007/s12541-019-00103-2.

[11] A. Waldbaur, H. Rapp, K. Länge, and B. E. Rapp, "Let there be chip—towards rapid prototyping of microfluidic devices: one-step manufacturing processes," *Anal. Methods*, vol. 3, no. 12, pp. 2681–2716, Dec. 2011, doi: 10.1039/C1AY05253E.

[12] C. Iliescu, H. Taylor, M. Avram, J. Miao, and S. Franssila, "A practical guide for the fabrication of microfluidic devices using glass and silicon," *Biomicrofluidics*, vol. 6, no. 1, 2012.

[13] K. L. Wlodarczyk *et al.*, "Rapid laser manufacturing of microfluidic devices from glass substrates," *Micromachines*, vol. 9, no. 8, p. 409, 2018.

[14] J. C. Bertolini, "Hydrofluoric acid: A review of toxicity," *J. Emerg. Med.*, vol. 10, no. 2, pp. 163–168, Mar. 1992, doi: 10.1016/0736-4679(92)90211-B.

[15] G. S. Fiorini and D. T. Chiu, "Disposable microfluidic devices: fabrication, function, and application," *BioTechniques*, vol. 38, no. 3, pp. 429–446, 2005.

[16] D. J. Guckenberger, T. E. de Groot, A. M. D. Wan, D. J. Beebe, and E. W. K. Young, "Micromilling: a method for ultra-rapid prototyping of plastic microfluidic devices," *Lab. Chip*, vol. 15, no. 11, pp. 2364–2378, May 2015, doi: 10.1039/C5LC00234F.

[17] V. Faustino, S. O. Catarino, R. Lima, and G. Minas, “Biomedical microfluidic devices by using low-cost fabrication techniques: A review,” *J. Biomech.*, vol. 49, no. 11, pp. 2280–2292, Jul. 2016, doi: 10.1016/j.jbiomech.2015.11.031.

[18] M. Islam, R. Natu, and R. Martinez-Duarte, “A study on the limits and advantages of using a desktop cutter plotter to fabricate microfluidic networks,” *Microfluid. Nanofluidics*, vol. 19, no. 4, pp. 973–985, Oct. 2015, doi: 10.1007/s10404-015-1626-9.

[19] S. Kojić *et al.*, “Optimization of hybrid microfluidic chip fabrication methods for biomedical application,” *Microfluid. Nanofluidics*, vol. 24, no. 9, p. 66, 2020.

[20] M. Koch, A. Evans, and A. Brunnschweiler, *Microfluidic technology and applications*. in Microtechnologies and microsystems series, no. 1. Philadelphia, PA: Research Studies Press, 2000.

[21] V. Srinivasan, V. K. Pamula, and R. B. Fair, “Droplet-based microfluidic lab-on-a-chip for glucose detection,” *Anal. Chim. Acta*, vol. 507, no. 1, pp. 145–150, Apr. 2004, doi: 10.1016/j.aca.2003.12.030.

[22] D. J. Rowe, A. Porch, D. A. Barrow, and C. J. Allender, “Microfluidic device for compositional analysis of solvent systems at microwave frequencies,” *Sens. Actuators B Chem.*, vol. 169, pp. 213–221, Jul. 2012, doi: 10.1016/j.snb.2012.04.069.

[23] H. Shi, K. Nie, B. Dong, M. Long, H. Xu, and Z. Liu, “Recent progress of microfluidic reactors for biomedical applications,” *Chem. Eng. J.*, vol. 361, pp. 635–650, Apr. 2019, doi: 10.1016/j.cej.2018.12.104.

[24] H. Yun, K. Kim, and W. G. Lee, “Cell manipulation in microfluidics,” *Biofabrication*, vol. 5, no. 2, p. 022001, Feb. 2013, doi: 10.1088/1758-5082/5/2/022001.

[25] M. Zhang and S. Li, “Controllable liquid colour-changing lenses with microfluidic channels for vision protection, camouflage and optical filtering based on soft lithography fabrication,” *SpringerPlus*, vol. 5, no. 1, p. 580, Dec. 2016, doi: 10.1186/s40064-016-2231-4.

[26] J. Wu, G. Zheng, and L. Man Lee, “Optical imaging techniques in microfluidics and their applications,” *Lab. Chip*, vol. 12, no. 19, pp. 3566–3575, 2012, doi: 10.1039/C2LC40517B.

[27] J. Fuentes-Fernández, S. Cuevas, L. C. Álvarez-Nuñez, and A. Watson, “Tests and evaluation of a variable focus liquid lens for curvature wavefront sensors in astronomy,” *Appl. Opt.*, vol. 52, no. 30, pp. 7256–7264, Oct. 2013, doi: 10.1364/AO.52.007256.

[28] P. Mach *et al.*, “Tunable microfluidic optical fiber,” *Appl. Phys. Lett.*, vol. 80, no. 23, pp. 4294–4296, Jun. 2002, doi: 10.1063/1.1483384.

[29] K. Kobayashi and H. Onoe, “Microfluidic-based flexible reflective multicolor display,” *Microsyst. Nanoeng.*, vol. 4, no. 1, Art. no. 1, Jul. 2018, doi: 10.1038/s41378-018-0018-1.

[30] S. A. Morin, R. F. Shepherd, S. W. Kwok, A. A. Stokes, A. Nemiroski, and G. M. Whitesides, “Camouflage and Display for Soft Machines,” *Science*, vol. 337, no. 6096, pp. 828–832, Aug. 2012, doi: 10.1126/science.1222149.

[31] L. Li, H. Li, and S. Li, “Study on the Discoloration Mechanism of Cavity Type Microfluidic Camouflage Film,” in *2022 IEEE International Conference on Electrical Engineering, Big Data and Algorithms (EEBDA)*, Feb. 2022, pp. 303–307. doi: 10.1109/EEBDA53927.2022.9744810.

[32] K. Raj M and S. Chakraborty, “PDMS microfluidics: A mini review,” *J. Appl. Polym. Sci.*, vol. 137, no. 27, p. 48958, 2020, doi: 10.1002/app.48958.

[33] J. C. McDonald and G. M. Whitesides, "Poly(dimethylsiloxane) as a Material for Fabricating Microfluidic Devices," *Acc. Chem. Res.*, vol. 35, no. 7, pp. 491–499, Jul. 2002, doi: 10.1021/ar010110q.

[34] J. C. McDonald *et al.*, "Fabrication of Microfluidic Systems in Poly(dimethylsiloxane)," *Electrophoresis*, vol. 21, pp. 27–40, 2000.

[35] C. Hu *et al.*, "A one-step strategy for ultra-fast and low-cost mass production of plastic membrane microfluidic chips," *Lab. Chip*, vol. 16, no. 20, pp. 3909–3918, Oct. 2016, doi: 10.1039/C6LC00957C.

[36] E. Team, "PDMS: A review," *Elveflow*, Feb. 2021, Accessed: Dec. 06, 2022. [Online]. Available: https://www.elveflow.com/microfluidic-reviews/general-microfluidics/the-polydimethylsiloxane-pdms-and-microfluidics/

[37] E. Roy, M. Geissler, J.-C. Galas, and T. Veres, "Prototyping of microfluidic systems using a commercial thermoplastic elastomer," *Microfluid. Nanofluidics*, vol. 11, no. 3, pp. 235–244, Sep. 2011, doi: 10.1007/s10404-011-0789-2.

[38] K. Liu *et al.*, "Programmable Microfluidics for Dynamic Multiband Camouflage," In Review, preprint, Jul. 2022. doi: 10.21203/rs.3.rs-1745947/v1.

[39] X. Sun *et al.*, "Low-Cost and High-Speed Fabrication of Camouflage-Enabling Microfluidic Devices using Ultrahigh Molecular Weight Polyethylene," *Adv. Mater. Technol.*, vol. n/a, no. n/a, p. 2300705, doi: 10.1002/admt.202300705.

[40] X. Hou *et al.*, "Interplay between materials and microfluidics," *Nat. Rev. Mater.*, vol. 2, no. 5, Art. no. 5, Apr. 2017, doi: 10.1038/natrevmats.2017.16.

[41] P. N. Nge, C. I. Rogers, and A. T. Woolley, "Advances in Microfluidic Materials, Functions, Integration, and Applications," *Chem. Rev.*, vol. 113, no. 4, pp. 2550–2583, Apr. 2013, doi: 10.1021/cr300337x.

[42] C. K. Fredrickson and Z. Hugh Fan, "Macro-to-micro interfaces for microfluidic devices," *Lab. Chip*, vol. 4, no. 6, pp. 526–533, 2004, doi: 10.1039/B410720A.

[43] A. Puntambekar and C. H. Ahn, "Self-aligning microfluidic interconnects for glass- and plastic-based microfluidic systems," *J. Micromechanics Microengineering*, vol. 12, no. 1, p. 35, Dec. 2001, doi: 10.1088/0960-1317/12/1/306.

[44] H. Chen, D. Acharya, A. Gajraj, and J.-C. Meiners, "Robust Interconnects and Packaging for Microfluidic Elastomeric Chips," *Anal. Chem.*, vol. 75, no. 19, pp. 5287–5291, Oct. 2003, doi: 10.1021/ac034179i.

[45] J. Liu, C. Hansen, and S. R. Quake, "Solving the 'World-to-Chip' Interface Problem with a Microfluidic Matrix," *Anal. Chem.*, vol. 75, no. 18, pp. 4718–4723, Sep. 2003, doi: 10.1021/ac0346407.

[46] Y. Temiz, R. D. Lovchik, G. V. Kaigala, and E. Delamarche, "Lab-on-a-chip devices: How to close and plug the lab?," *Microelectron. Eng.*, vol. 132, pp. 156–175, Jan. 2015, doi: 10.1016/j.mee.2014.10.013.

[47] R. M. Patel, "2 - Polyethylene," in *Multilayer Flexible Packaging (Second Edition)*, J. R. Wagner, Ed., in Plastics Design Library. , William Andrew Publishing, 2016, pp. 17–34. doi: 10.1016/B978-0-323-37100-1.00002-8.

[48] S. Ronca, "Chapter 10 - Polyethylene," in *Brydson's Plastics Materials (Eighth Edition)*, M. Gilbert, Ed., Butterworth-Heinemann, 2017, pp. 247–278. doi: 10.1016/B978-0-323-35824-8.00010-4.

[49] Z. Yao, H. J. Seong, and Y.-S. Jang, "Environmental toxicity and decomposition of polyethylene," *Ecotoxicol. Environ. Saf.*, vol. 242, p. 113933, Sep. 2022, doi: 10.1016/j.ecoenv.2022.113933.

[50] S. L. Aggarwal and O. J. Sweeting, "Polyethylene: Preparation, Structure, And Properties," *Chem. Rev.*, vol. 57, no. 4, pp. 665–742, Aug. 1957, doi: 10.1021/cr50016a004.

[51] C. Vasile and M. Pascu, *Practical Guide to Polyethylene*. iSmithers Rapra Publishing, 2005.

[52] E. W. Fawcett, "Polymerisation of ethylene," *Trans Faraday Soc*, vol. 32, pp. 119–129, 1936.

[53] F. E. William, G. R. Oswald, and P. M. Willcox, "Polymerization of olefins," US2153553A, Apr. 11, 1939 Accessed: Oct. 22, 2023. [Online]. Available: https://patents.google.com/patent/US2153553A/en

[54] H. J. Paul and R. L. Banks, "Polymers and production thereof," US2825721A, Mar. 04, 1958 Accessed: Oct. 22, 2023. [Online]. Available: https://patents.google.com/patent/US2825721A/en

[55] M. P. McDaniel, "A review of the Phillips supported chromium catalyst and its commercial use for ethylene polymerization," *Adv. Catal.*, vol. 53, pp. 123–606, 2010.

[56] G. Natta *et al.*, "Crystalline high polymers of α-olefins," *J. Am. Chem. Soc.*, vol. 77, no. 6, pp. 1708–1710, 1955.

[57] K. Ziegler, E. Holzkamp, H. Breil, and H. Martin, "Polymerisation von Äthylen und anderen Olefinen," *Angew. Chem.*, vol. 67, no. 16, pp. 426–426, Aug. 1955, doi: 10.1002/ange.19550671610.

[58] E. F. Peters, Alex. Zletz, and B. L. Evering, "Solid Catalysts in Ethylene Polymerization," *Ind. Eng. Chem.*, vol. 49, no. 11, pp. 1879–1882, Nov. 1957, doi: 10.1021/ie50575a035.

[59] J. P. Hogan, E. T. Hsieh, and J. C. Randall, "Low density polyethylene," US4522987A, Jun. 11, 1985 Accessed: Oct. 22, 2023. [Online]. Available: https://patents.google.com/patent/US4522987A/en

[60] E. A. Benham, P. D. Smith, and M. P. McDaniel, "A process for the simultaneous oligomerization and copolymerization of ethylene," *Polym. Eng. Sci.*, vol. 28, no. 22, pp. 1469–1472, 1988, doi: 10.1002/pen.760282206.

[61] S. M. Kurtz, *The UHMWPE Handbook: Ultra-High Molecular Weight Polyethylene in Total Joint Replacement*. Elsevier, 2004.

[62] N. C. Paxton, M. C. Allenby, P. M. Lewis, and M. A. Woodruff, "Biomedical applications of polyethylene," *Eur. Polym. J.*, vol. 118, pp. 412–428, Sep. 2019, doi: 10.1016/j.eurpolymj.2019.05.037.

[63] P. M. Visakh, "Chapter 1 - Polyaniline-Based Blends, Composites, and Nanocomposites: State of the Art, New Challenges, and Opportunities," in *Polyaniline Blends, Composites, and Nanocomposites*, P. M. Visakh, C. D. Pina, and E. Falletta, Eds., Elsevier, 2018, pp. 1–22. doi: 10.1016/B978-0-12-809551-5.00001-1.

[64] K. Patel, S. H. Chikkali, and S. Sivaram, "Ultrahigh molecular weight polyethylene: Catalysis, structure, properties, processing and applications," *Prog. Polym. Sci.*, vol. 109, p. 101290, Oct. 2020, doi: 10.1016/j.progpolymsci.2020.101290.

[65] "Standard Specification for Ultra-High-Molecular-Weight Polyethylene Molding and Extrusion Materials." Accessed: Oct. 22, 2023. [Online]. Available: https://www.astm.org/d4020-01.html

[66] K. Friedrich, "Polymer composites for tribological applications," *Adv. Ind. Eng. Polym. Res.*, vol. 1, no. 1, pp. 3–39, 2018.

[67] K. K. Karuppiah *et al.*, "Friction and wear behavior of ultra-high molecular weight polyethylene as a function of polymer crystallinity," *Acta Biomater.*, vol. 4, no. 5, pp. 1401–1410, 2008.

[68] M. C. Sobieraj and C. M. Rimnac, "Ultra high molecular weight polyethylene: mechanics, morphology, and clinical behavior," *J. Mech. Behav. Biomed. Mater.*, vol. 2, no. 5, pp. 433–443, 2009.

[69] L. G. Amurin *et al.*, "Multifunctionality in ultra high molecular weight polyethylene nanocomposites with reduced graphene oxide: Hardness, impact and tribological properties," *Polymer*, vol. 240, p. 124475, Feb. 2022, doi: 10.1016/j.polymer.2021.124475.

[70] G. Lippmann, "Relations entre les phénomènes électriques et capillaires," *Ann Chim Phys*, vol. 5, no. 11, pp. 494–549, 1875.

[71] Y.-P. Zhao and Y. Wang, "Fundamentals and Applications of Electrowetting," *Rev. Adhes. Adhes.*, vol. 1, no. 1, pp. 114–174, Feb. 2013, doi: 10.7569/RAA.2013.097304.

[72] F. Mugele and J.-C. Baret, "Electrowetting: from basics to applications," *J. Phys. Condens. Matter*, vol. 17, no. 28, p. R705, Jul. 2005, doi: 10.1088/0953-8984/17/28/R01.

[73] C. Quilliet and B. Berge, "Electrowetting: a recent outbreak," *Curr. Opin. Colloid Interface Sci.*, vol. 6, no. 1, pp. 34–39, Feb. 2001, doi: 10.1016/S1359-0294(00)00085-6.

[74] A. Frumkin, A. Gorodetskaya, B. Kabanov, and N. Nekrasov, "Electrocapillary phenomena and the wetting of metals by electrolytic solutions, I," *Phys Z Sowjetunion*, vol. 1, pp. 255–84, 1932.

[75] A. N. Frumkin and A. Gorodetzkaya, "On the phenomena of wetting and the adhesion of bubbles. II. The mechanism of the adhesion of bubbles to a mercury surface," *Acta Physicochim URSS*, vol. 9, p. 327, 1938.

[76] A. A. Papaderakis and R. A. W. Dryfe, "The renaissance of electrowetting," *Curr. Opin. Electrochem.*, vol. 38, p. 101245, Apr. 2023, doi: 10.1016/j.coelec.2023.101245.

[77] G. Beni and S. Hackwood, "Electro-wetting displays," *Appl. Phys. Lett.*, vol. 38, no. 4, pp. 207–209, 1981.

[78] J. L. Jackel, S. Hackwood, and G. Beni, "Electrowetting optical switch," *Appl. Phys. Lett.*, vol. 40, no. 1, pp. 4–5, Jan. 1982, doi: 10.1063/1.92920.

[79] P. Teng, D. Tian, H. Fu, and S. Wang, "Recent progress of electrowetting for droplet manipulation: from wetting to superwetting systems," *Mater. Chem. Front.*, vol. 4, no. 1, pp. 140–154, 2020, doi: 10.1039/C9QM00458K.

[80] J. A. M. Sondag-Huethorst and L. G. J. Fokkink, "Electrical double layers on thiol-modified polycrystalline gold electrodes," *J. Electroanal. Chem.*, vol. 367, no. 1–2, pp. 49–57, 1994.

[81] J. A. M. Sondag-Huethorst and L. G. J. Fokkink, "Potential-dependent wetting of electroactive ferrocene-terminated alkanethiolate monolayers on gold," *Langmuir*, vol. 10, no. 11, pp. 4380–4387, 1994.

[82] R. A. Bernhoft, "Mercury Toxicity and Treatment: A Review of the Literature," *J. Environ. Public Health*, vol. 2012, p. e460508, Dec. 2011, doi: 10.1155/2012/460508.

[83] B. Berge, "Electrocapillarity and wetting of insulator films by water," *Comptes Rendus Acad. Sci. Ser. Ii*, vol. 317, no. 2, pp. 157–163, 1993.

[84] B. Berge and J. Peseux, *Lens with variable focus*. Google Patents, 2002.

[85] B. Berge and J. Peseux, “Variable focal lens controlled by an external voltage: An application of electrowetting,” *Eur. Phys. J. E*, vol. 3, no. 2, pp. 159–163, Oct. 2000, doi: 10.1007/s101890070029.

[86] S. Kuiper and B. H. Hendriks, “Variable-focus liquid lens for miniature cameras,” *Appl. Phys. Lett.*, vol. 85, no. 7, pp. 1128–1130, 2004.

[87] N. Binh-Khiem, K. Matsumoto, and I. Shimoyama, “Polymer thin film deposited on liquid for varifocal encapsulated liquid lenses,” *Appl. Phys. Lett.*, vol. 93, no. 12, p. 124101, Sep. 2008, doi: 10.1063/1.2988467.

[88] R. A. Hayes and B. J. Feenstra, “Video-speed electronic paper based on electrowetting,” *Nature*, vol. 425, no. 6956, Art. no. 6956, Sep. 2003, doi: 10.1038/nature01988.

[89] B. Sun, K. Zhou, Y. Lao, J. Heikenfeld, and W. Cheng, “Scalable fabrication of electrowetting displays with self-assembled oil dosing,” *Appl. Phys. Lett.*, vol. 91, no. 1, 2007.

[90] B. J. Feenstra, R. A. Hayes, and M. W. J. Prins, “Display device,” US8213071B2, Jul. 03, 2012 Accessed: Aug. 11, 2023. [Online]. Available: https://patents.google.com/patent/US8213071/en

[91] D. Y. Kim, M.-J. Kim, G. Sung, and J.-Y. Sun, “Stretchable and reflective displays: materials, technologies and strategies,” *Nano Converg.*, vol. 6, no. 1, p. 21, Jun. 2019, doi: 10.1186/s40580-019-0190-5.

[92] M. G. Pollack, A. D. Shenderov, and R. B. Fair, “Electrowetting-based actuation of droplets for integrated microfluidics,” *Lab. Chip*, vol. 2, no. 2, pp. 96–101, 2002, doi: 10.1039/B110474H.

[93] S. K. Cho, H. Moon, and C.-J. Kim, “Creating, transporting, cutting, and merging liquid droplets by electrowetting-based actuation for digital microfluidic circuits,” *J. Microelectromechanical Syst.*, vol. 12, no. 1, pp. 70–80, Feb. 2003, doi: 10.1109/JMEMS.2002.807467.

[94] R. S. Sista, A. E. Eckhardt, V. Srinivasan, M. G. Pollack, S. Palanki, and V. K. Pamula, “Heterogeneous immunoassays using magnetic beads on a digital microfluidic platform,” *Lab. Chip*, vol. 8, no. 12, pp. 2188–2196, Dec. 2008, doi: 10.1039/B807855F.

[95] J. Li and Chang-Jin “CJ” Kim, “Current commercialization status of electrowetting-on-dielectric (EWOD) digital microfluidics,” *Lab. Chip*, vol. 20, no. 10, pp. 1705–1712, 2020, doi: 10.1039/D0LC00144A.

[96] T. Yamamoto, M. Doi, and D. Andelman, “Contact angle saturation in electrowetting: Injection of ions into the surrounding media,” *Europhys. Lett.*, vol. 112, no. 5, p. 56001, Dec. 2015, doi: 10.1209/0295-5075/112/56001.

[97] M. Vallet, M. Vallade, and B. Berge, “Limiting phenomena for the spreading of water on polymer films by electrowetting,” *Eur. Phys. J. B - Condens. Matter Complex Syst.*, vol. 11, no. 4, pp. 583–591, Oct. 1999, doi: 10.1007/s100510051186.

[98] S. Chevalliot, S. Kuiper, and J. Heikenfeld, “Experimental validation of the invariance of electrowetting contact angle saturation,” *J. Adhes. Sci. Technol.*, vol. 26, no. 12–17, pp. 1909–1930, 2012.

[99] F. Mugele, “Fundamental challenges in electrowetting: from equilibrium shapes to contact angle saturation and drop dynamics,” *Soft Matter*, vol. 5, no. 18, pp. 3377–3384, Sep. 2009, doi: 10.1039/B904493K.

[100] A. I. Drygiannakis, A. G. Papathanasiou, and A. G. Boudouvis, “On the connection between dielectric breakdown strength, trapping of charge, and contact angle saturation in electrowetting,” *Langmuir*, vol. 25, no. 1, pp. 147–152, 2009.

[101] A. Quinn, R. Sedev, and J. Ralston, “Contact Angle Saturation in Electrowetting,” *J. Phys. Chem. B*, vol. 109, no. 13, pp. 6268–6275, Apr. 2005, doi: 10.1021/jp040478f.

[102] D. Klarman, D. Andelman, and M. Urbakh, “A model of electrowetting, reversed electrowetting, and contact angle saturation,” *Langmuir*, vol. 27, no. 10, pp. 6031–6041, 2011.

[103] H. A. A. Ali, H. A. Mohamed, and M. Abdelgawad, “Repulsion-based model for contact angle saturation in electrowetting,” *Biomicrofluidics*, vol. 9, no. 1, 2015.

[104] A. G. Papathanasiou and A. G. Boudouvis, “Manifestation of the connection between dielectric breakdown strength and contact angle saturation in electrowetting,” *Appl. Phys. Lett.*, vol. 86, no. 16, 2005.

[105] M. Stevens and S. Merilaita, “Animal camouflage: current issues and new perspectives,” *Philos. Trans. R. Soc. B Biol. Sci.*, vol. 364, no. 1516, pp. 423–427, Feb. 2009, doi: 10.1098/rstb.2008.0217.

[106] M. Stevens, I. C. Cuthill, A. M. M. Windsor, and H. J. Walker, “Disruptive contrast in animal camouflage,” *Proc. R. Soc. B Biol. Sci.*, vol. 273, no. 1600, pp. 2433–2438, Oct. 2006, doi: 10.1098/rspb.2006.3614.

[107] R. Hanlon, “Cephalopod dynamic camouflage,” *Curr. Biol.*, vol. 17, no. 11, pp. R400–R404, Jun. 2007, doi: 10.1016/j.cub.2007.03.034.

[108] C. J. Lin, Y. T. Prasetyo, N. D. Siswanto, and B. C. Jiang, “Optimization of color design for military camouflage in CIELAB color space,” *Color Res. Appl.*, vol. 44, no. 3, pp. 367–380, 2019, doi: 10.1002/col.22352.

[109] L. Talas, R. J. Baddeley, and I. C. Cuthill, “Cultural evolution of military camouflage,” *Philos. Trans. R. Soc. B Biol. Sci.*, vol. 372, no. 1724, p. 20160351, Jul. 2017, doi: 10.1098/rstb.2016.0351.

[110] M. Friškovec and H. Gabrijelčič, “Development of a procedure for camouflage pattern design,” *Fibres Text. East. Eur.*, vol. 18, no. 4, p. 81, 2010.

[111] X. Wei, G. Li, and K. Wang, “A Novel Method for Automatic Camouflage Pattern Synthesize,” *IEEE Access*, vol. 9, pp. 67559–67568, 2021, doi: 10.1109/ACCESS.2021.3077258.

[112] F. Steffens, S. E. Gralha, I. L. S. Ferreira, and F. R. Oliveira, “Military Textiles - An Overview of New Developments,” *Key Eng. Mater.*, vol. 812, pp. 120–126, Jul. 2019, doi: 10.4028/www.scientific.net/KEM.812.120.

[113] S. M. Burkinshaw, G. Hallas, and A. D. Towns, “Infrared camouflage,” *Rev. Prog. Color. Relat. Top.*, vol. 26, no. 1, pp. 47–53, 1996, doi: 10.1111/j.1478-4408.1996.tb00109.x.

[114] L. M. Degenstein, D. Sameoto, J. D. Hogan, A. Asad, and P. I. Dolez, “Smart Textiles for Visible and IR Camouflage Application: State-of-the-Art and Microfabrication Path Forward,” *Micromachines*, vol. 12, no. 7, Art. no. 7, Jul. 2021, doi: 10.3390/mi12070773.

[115] A. R. Horrocks and S. C. Anand, *Handbook of Technical Textiles*. Elsevier, 2000.

[116] S. Chandra, D. Franklin, J. Cozart, A. Safaei, and D. Chanda, “Adaptive Multispectral Infrared Camouflage,” *ACS Photonics*, vol. 5, no. 11, pp. 4513–4519, Nov. 2018, doi: 10.1021/acsphotonics.8b00972.

[117] X. Liu and W. J. Padilla, “Thermochromic infrared metamaterials,” *Adv. Mater.*, vol. 28, no. 5, pp. 871–875, 2016.

[118] X. Liu and W. J. Padilla, “Artificial electrochromic & thermochromic infrared metamaterials,” in *2015 International Conference on Optical MEMS and Nanophotonics (OMN)*, IEEE, 2015, pp. 1–2.

[119] Y. Tian *et al.*, “A comprehensive study of electrochromic device with variable infrared emissivity based on polyaniline conducting polymer,” *Sol. Energy Mater. Sol. Cells*, vol. 170, pp. 120–126, 2017.

[120] L. Xiao *et al.*, “Fast Adaptive Thermal Camouflage Based on Flexible VO2/Graphene/CNT Thin Films,” *Nano Lett.*, vol. 15, no. 12, pp. 8365–8370, Dec. 2015, doi: 10.1021/acs.nanolett.5b04090.

[121] H. Pisavadia, A. Asad, D. Sameoto, P. Dolez, and J. D. Hogan, “Design of micro- and macro-scale polymeric metamaterial solutions for passive and active thermal camouflaging applications,” *Nano Sel.*, vol. 4, no. 4, pp. 263–270, 2023, doi: 10.1002/nano.202200212.

[122] B. Kuswandi, Nuriman, J. Huskens, and W. Verboom, “Optical sensing systems for microfluidic devices: A review,” *Anal. Chim. Acta*, vol. 601, no. 2, pp. 141–155, Oct. 2007, doi: 10.1016/j.aca.2007.08.046.

[123] P. Cui and S. Wang, “Application of microfluidic chip technology in pharmaceutical analysis: A review,” *J. Pharm. Anal.*, vol. 9, no. 4, pp. 238–247, Aug. 2019, doi: 10.1016/j.jpha.2018.12.001.

[124] G. Weisgrab, A. Ovsianikov, and P. F. Costa, “Functional 3D Printing for Microfluidic Chips,” *Adv. Mater. Technol.*, vol. 4, no. 10, p. 1900275, 2019, doi: 10.1002/admt.201900275.

[125] M. Stevens and S. Merilaita, *Animal Camouflage: Mechanisms and Function*. Cambridge University Press, 2011.

[126] A. King, “The digital revolution: Camouflage in the twenty-first century,” *Millennium*, vol. 42, no. 2, pp. 397–424, Jan. 2014, doi: 10.1177/0305829813512885.

[127] M. Zhang and S. Li, “Low-cost and facile implementation of microfluidic colour-changing devices using dry film photoresist-based moulds,” *J. Exp. Nanosci.*, vol. 13, no. 1, pp. 221–230, Jan. 2018, doi: 10.1080/17458080.2018.1509382.

[128] S. M. Scott and Z. Ali, “Fabrication Methods for Microfluidic Devices: An Overview,” *Micromachines*, vol. 12, no. 3, Art. no. 3, Mar. 2021, doi: 10.3390/mi12030319.

[129] D. I. Walsh, D. S. Kong, S. K. Murthy, and P. A. Carr, “Enabling Microfluidics: from Clean Rooms to Makerspaces,” *Trends Biotechnol.*, vol. 35, no. 5, pp. 383–392, May 2017, doi: 10.1016/j.tibtech.2017.01.001.

[130] D. A. Bartholomeusz, R. W. Boutte, and J. D. Andrade, “Xurography: rapid prototyping of microstructures using a cutting plotter,” *J. Microelectromechanical Syst.*, vol. 14, no. 6, pp. 1364–1374, Dec. 2005, doi: 10.1109/JMEMS.2005.859087.

[131] J. Canny, “A Computational Approach to Edge Detection,” *IEEE Trans. Pattern Anal. Mach. Intell.*, vol. PAMI-8, no. 6, pp. 679–698, Nov. 1986, doi: 10.1109/TPAMI.1986.4767851.

[132] L. Ding and A. Goshtasby, “On the Canny edge detector,” *Pattern Recognit.*, vol. 34, no. 3, pp. 721–725, Mar. 2001, doi: 10.1016/S0031-3203(00)00023-6.

[133] Y. Luo and R. Duraiswami, “Canny edge detection on NVIDIA CUDA,” in *2008 IEEE Computer Society Conference on Computer Vision and Pattern Recognition Workshops*, Jun. 2008, pp. 1–8. doi: 10.1109/CVPRW.2008.4563088.

[134] S. Süsstrunk, R. Buckley, and S. Swen, “Standard RGB color spaces,” in *Proc. IS&T;/SID 7th Color Imaging Conference*, 1999, pp. 127–134.

[135] M. Chen, D. Pang, and H. Yan, “Highly solar reflectance and infrared transparent porous coating for non-contact heat dissipations,” *iScience*, vol. 25, no. 8, p. 104726, Jul. 2022, doi: 10.1016/j.isci.2022.104726.

[136] R. J. Denning, “15 - Camouflage fabrics,” in *Engineering of High-Performance Textiles*, M. Miao and J. H. Xin, Eds., in The Textile Institute Book Series. , Woodhead Publishing, 2018, pp. 349–375. doi: 10.1016/B978-0-08-101273-4.00016-0.

[137] W. Przybył, W. Radosz, and A. Januszko, “Colour management system: Monte Carlo implementation for camouflage pattern generation,” *Color. Technol.*, vol. 136, no. 5, pp. 407–416, 2020, doi: 10.1111/cote.12483.

[138] M. Kobayashi, A. Ono, M. Otsuki, H. Sakate, and F. Sakuma, “A Database of Normal Spectral Emissivities of Metals at High Temperatures,” *Int. J. Thermophys.*, vol. 20, no. 1, pp. 299–308, Jan. 1999, doi: 10.1023/A:1021467322442.

[139] C. Hu *et al.*, “New design for highly durable infrared-reflective coatings,” *Light Sci. Appl.*, vol. 7, no. 4, Art. no. 4, Apr. 2018, doi: 10.1038/lsa.2017.175.

[140] J. Liu, M. Wang, S. Chen, and M. O. Robbins, “Uncovering Molecular Mechanisms of Electrowetting and Saturation with Simulations,” *Phys. Rev. Lett.*, vol. 108, no. 21, p. 216101, May 2012, doi: 10.1103/PhysRevLett.108.216101.

[141] G. McHale, C. V. Brown, and N. Sampara, “Voltage-induced spreading and superspreading of liquids,” *Nat. Commun.*, vol. 4, no. 1, Art. no. 1, Mar. 2013, doi: 10.1038/ncomms2619.

[142] O. Caro-Pérez, J. Casals-Terré, and M. B. Roncero, “Materials and Manufacturing Methods for EWOD Devices: Current Status and Sustainability Challenges,” *Macromol. Mater. Eng.*, vol. 308, no. 1, p. 2200193, 2023, doi: 10.1002/mame.202200193.

[143] H. Moon, S. K. Cho, R. L. Garrell, and C.-J. “Cj” Kim, “Low voltage electrowetting-on-dielectric,” *J. Appl. Phys.*, vol. 92, no. 7, pp. 4080–4087, Oct. 2002, doi: 10.1063/1.1504171.

[144] C. B. Eaker, I. D. Joshipura, L. R. Maxwell, J. Heikenfeld, and M. D. Dickey, “Electrowetting without external voltage using paint-on electrodes,” *Lab. Chip*, vol. 17, no. 6, pp. 1069–1075, 2017, doi: 10.1039/C6LC01500J.

[145] I. Khan, S. Castelletto, and G. Rosengarten, “Deposition method and performance of SiO2 as a dielectric material for beam steering electrowetting devices,” *Mater. Res. Express*, vol. 5, no. 7, p. 076304, Jul. 2018, doi: 10.1088/2053-1591/aad010.

[146] F. Ribet, L. De Pietro, N. Roxhed, and G. Stemme, “Gas diffusion and evaporation control using EWOD actuation of ionic liquid microdroplets for gas sensing applications,” *Sens. Actuators B Chem.*, vol. 267, pp. 647–654, Aug. 2018, doi: 10.1016/j.snb.2018.04.076.

[147] Y.-J. Ciou, H.-T. Lee, Y.-W. Lin, and D.-J. Yao, “Microfluidic patterning using a digital microfluidic system,” *AIP Adv.*, vol. 10, no. 12, p. 125115, Dec. 2020, doi: 10.1063/5.0012684.

[148] C. Palma and R. D. Deegan, “Droplet Translation Actuated by Photoelectrowetting,” *Langmuir*, vol. 34, no. 10, pp. 3177–3185, Mar. 2018, doi: 10.1021/acs.langmuir.7b03340.

[149] I. F. Guha, J. Kedzierski, and B. Abedian, “Low-voltage electrowetting on a lipid bilayer formed on hafnium oxide,” *Appl. Phys. Lett.*, vol. 99, no. 2, p. 024105, Jul. 2011, doi: 10.1063/1.3610462.

[150] J. T. Kedzierski, R. Batra, S. Berry, I. Guha, and B. Abedian, “Validation of the trapped charge model of electrowetting contact angle saturation on lipid bilayers,” *J. Appl. Phys.*, vol. 114, no. 2, p. 024901, Jul. 2013, doi: 10.1063/1.4812476.

[151] S. Han, “Molecular dynamics simulation of oleic acid/oleate bilayers: An atomistic model for a ufasome membrane,” *Chem. Phys. Lipids*, vol. 175–176, pp. 79–83, Oct. 2013, doi: 10.1016/j.chemphyslip.2013.08.004.

[152] M. D. Dickey, “Stretchable and Soft Electronics using Liquid Metals,” *Adv. Mater.*, vol. 29, no. 27, p. 1606425, 2017, doi: 10.1002/adma.201606425.

[153] A. M. Alper, *High Temperature Oxides: Oxides of Rare Earths, Titanium, Zirconium, Hafnium, Niobium and Tantalum*. Elsevier, 2013.

[154] A. Ghosh, “Scaling Laws,” in *Mechanics Over Micro and Nano Scales*, S. Chakraborty, Ed., New York, NY: Springer New York, 2011, pp. 61–94. doi: 10.1007/978-1-4419-9601-5_2.

[155] J. R. Davis, *Corrosion of Aluminum and Aluminum Alloys*. ASM International, 1999.

[156] V. S. Kulkarni and C. Shaw, “Chapter 6 - Aerosols and Nasal Sprays,” in *Essential Chemistry for Formulators of Semisolid and Liquid Dosages*, V. S. Kulkarni and C. Shaw, Eds., Boston: Academic Press, 2016, pp. 71–97. doi: 10.1016/B978-0-12-801024-2.00006-6.

[157] “Dodecane(112-40-3) IR2 spectrum.” Accessed: May 05, 2023. [Online]. Available: https://www.chemicalbook.com/SpectrumEN_112-40-3_IR2.htm

[158] T. M. Koller *et al.*, “Liquid Viscosity and Surface Tension of n-Dodecane, n-Octacosane, Their Mixtures, and a Wax between 323 and 573 K by Surface Light Scattering,” *J. Chem. Eng. Data*, vol. 62, no. 10, pp. 3319–3333, Oct. 2017, doi: 10.1021/acs.jced.7b00363.

[159] H. B. De Aguiar, M. L. Strader, A. G. de Beer, and S. Roke, “Surface structure of sodium dodecyl sulfate surfactant and oil at the oil-in-water droplet liquid/liquid interface: a manifestation of a nonequilibrium surface state,” *J. Phys. Chem. B*, vol. 115, no. 12, pp. 2970–2978, 2011.

[160] B. Huang, “Super-resolution optical microscopy: multiple choices,” *Curr. Opin. Chem. Biol.*, vol. 14, no. 1, pp. 10–14, Feb. 2010, doi: 10.1016/j.cbpa.2009.10.013.

[161] A. Yamashita, M. Fujii, and T. Kaneko, “Color Registration of Underwater Images for Underwater Sensing with Consideration of Light Attenuation,” in *Proceedings 2007 IEEE International Conference on Robotics and Automation*, Apr. 2007, pp. 4570–4575. doi: 10.1109/ROBOT.2007.364183.

[162] M. Li, D. Liu, H. Cheng, L. Peng, and M. Zu, “Manipulating metals for adaptive thermal camouflage,” *Sci. Adv.*, vol. 6, no. 22, p. eaba3494, May 2020, doi: 10.1126/sciadv.aba3494.

[163] “Water.” Accessed: Aug. 14, 2023. [Online]. Available: https://webbook.nist.gov/cgi/cbook.cgi?ID=C7732185&Type=IR-SPEC&Index=1

Appendix

Appendix A: Supporting information for Chapter two

Supporting Information

Low-Cost and High-Speed Fabrication of Camouflage-Enabling Microfluidic Devices using Ultra High Molecular Weight Polyethylene

Xiaoruo Sun[1], Asad Asad[1]*, Mehnab Ali[1], Luka Morita[1], Patricia I. Dolez[2], James D. Hogan[1], Dan Sameoto[1]*

[1] Department of Mechanical Engineering, University of Alberta, Edmonton, Canada

[2] Department of Human Ecology, University of Alberta, Edmonton, Canada

* Corresponding authors: Dan Sameoto (sameoto@ualberta.ca) & Asad Asad (aaasad@uaberta.ca)

Keywords: Microfluidic devices, Adaptive visible camouflage, Adaptive Infrared camouflage, Polyethylene, Flexible microfluidic devices.

Table A1. Summarizes the cutting settings of the Silhouette Cameo 4 craft cutter software for different channel configurations. These settings include blade number, force, speed, and pass. The blade determines the depth of the blade's cut, ranging from 1-10, with 10 being the deepest. The force setting controls the amount of pressure the blade applies vertically, while the speed setting controls how quickly the machine operates. The pass setting represents the number of times the machine cuts the pattern.

	W1, W2, and W3 Channel	**H2 and H3 Channel**	**Channel with Metal layer**
Blade Number	3	9	3
Force	20	30	20
Speed	4	4	4
Passes	1	1	1

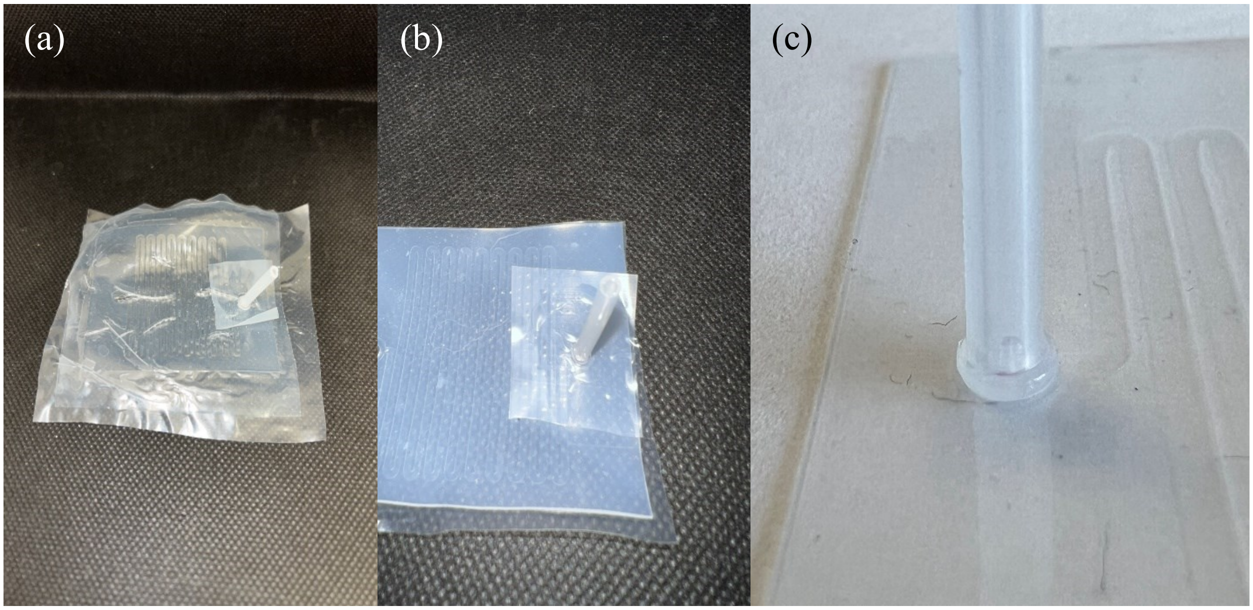

Figure A1. (a) early attempts at bonding UHMWPE without polyester resulted in buckling and wrinkling of the sheet, which often led to damage or blockage of the microfluidic channel. Furthermore, the early macro-to-micro interface tubing technique depicted in (a) and (b) was complex and unreliable, frequently resulting in permanent sealing of the inlet and outlet or significant leakage. However, significant progress has been made in the design of the interface, as demonstrated in (c). The current design features a robust PE tube thermally bonded to the UHMWPE microfluidic device with no leakage, thanks to the use of a polyester sheet that distributes force and eliminates buckling and wrinkling during the bonding process. This significant improvement in the design of the microfluidic device underscores the importance of continued optimization and refinement of fabrication processes in order to achieve reliable and durable microfluidic devices for a wide range of applications.

Figure A2. shows a microfluidic device microfluidic device with an incorporated metalized sheet.

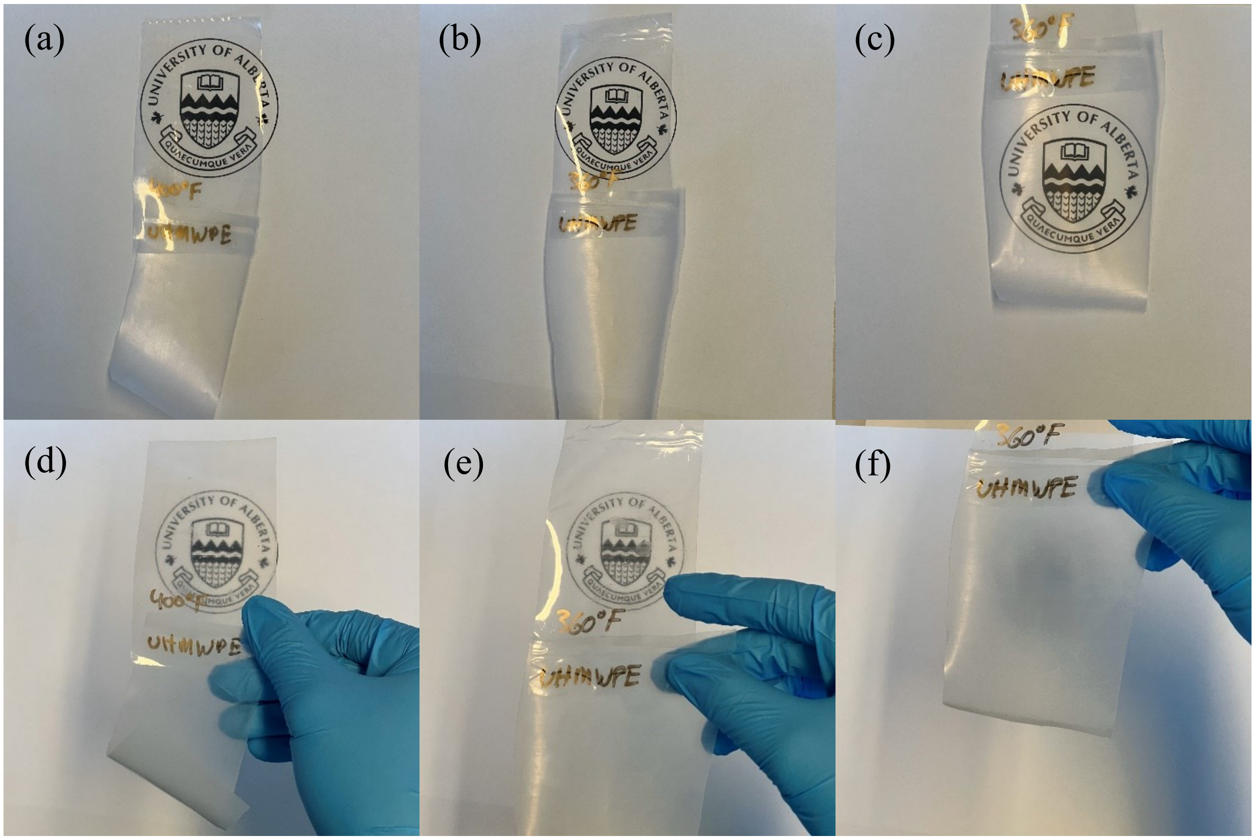

Figure A3. demonstrates the results of different surface treatment temperatures by heat-pressing a 100 µm UHMWPE sheet on a smooth surface such as Kapton tape or polyester sheet. The treatment reduces surface roughness and eliminates internal gaps in the UHMWPE. The treated and untreated UHMWPE sheets are then bonded using an impulse sealer, with the upper piece being the treated sheet and the lower piece being the original untreated sheet. The specimens were labeled with temperatures of 360°F and 400°F. The results show that there is no significant difference in transparency between the treated sheets at these two temperatures. However, there is a significant difference in transparency between the treated and untreated sheets. When placed directly on the University of Alberta logo, both the treated and untreated UHMWPE sheets allow the logo to be seen through them (as demonstrated in (a), (b), and (c)). However, when placed roughly 100 mm vertically away from the logo, the treated UHMWPE sheets still allow the logo to be visible (as shown in (d) and (e)), while the untreated UHMWPE sheet becomes opaque, and the logo is no longer visible (as shown in (f)).

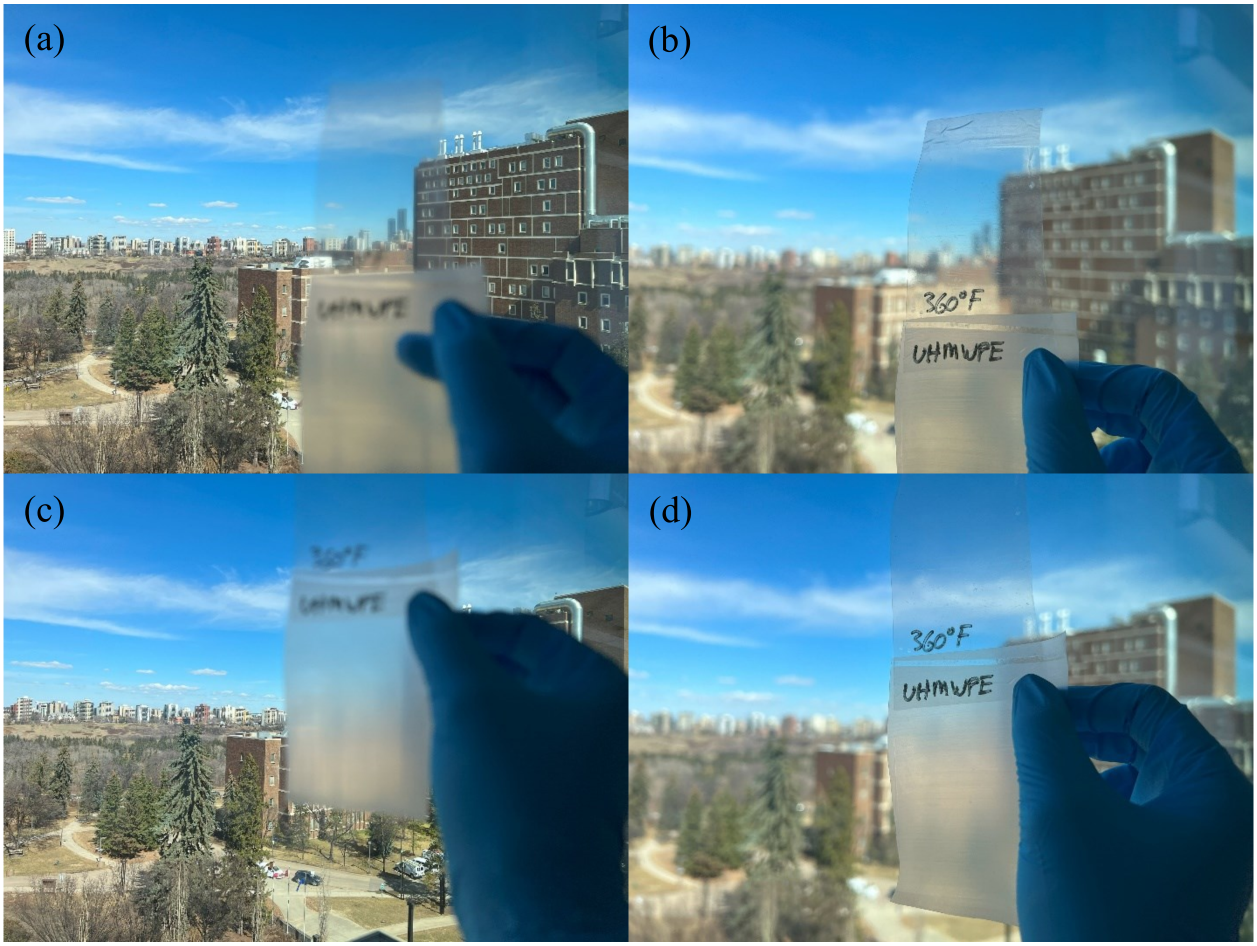

Figure A4. demonstrates the transparency comparison between treated and untreated UHMWPE sheets, confirming that the treated sheet has higher transparency. Panels (a) and (c) show the far building through the treated sheet, while panels (b) and (d) focus on the sheet itself. The untreated sheet is opaque, while the scenes outside the University of Alberta window are visible only through the treated UHMWPE sheet.

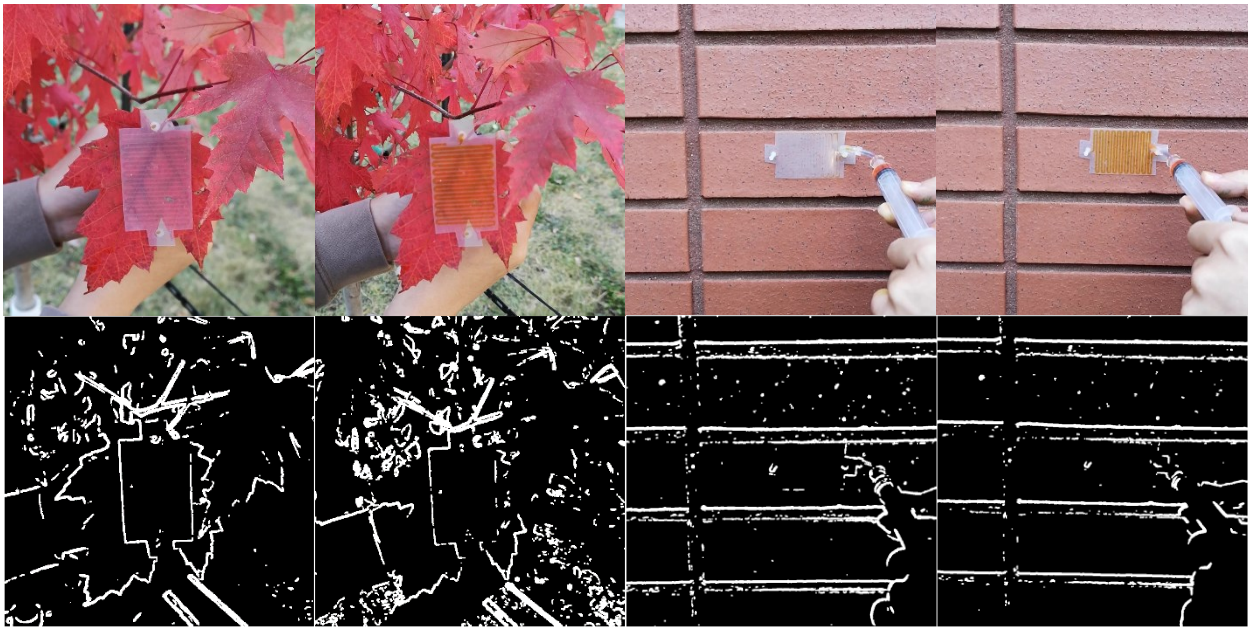

Figure A5. shows the Canny edge-finding algorithm analysis results for the brick and leaf backgrounds. The results for these two backgrounds were not significant since the canny edge finding algorithm was only suitable for some certain environments. With these two backgrounds, only the major edges were detected, the microfluidic device demonstrated no major improvements in terms of edge hiding. However, this result still demonstrated the microfluidic device cannot be detect by edge finding algorithm since the filled and unfilled device has very similar results, there is no detected edges within both the filled and unfilled device areas.

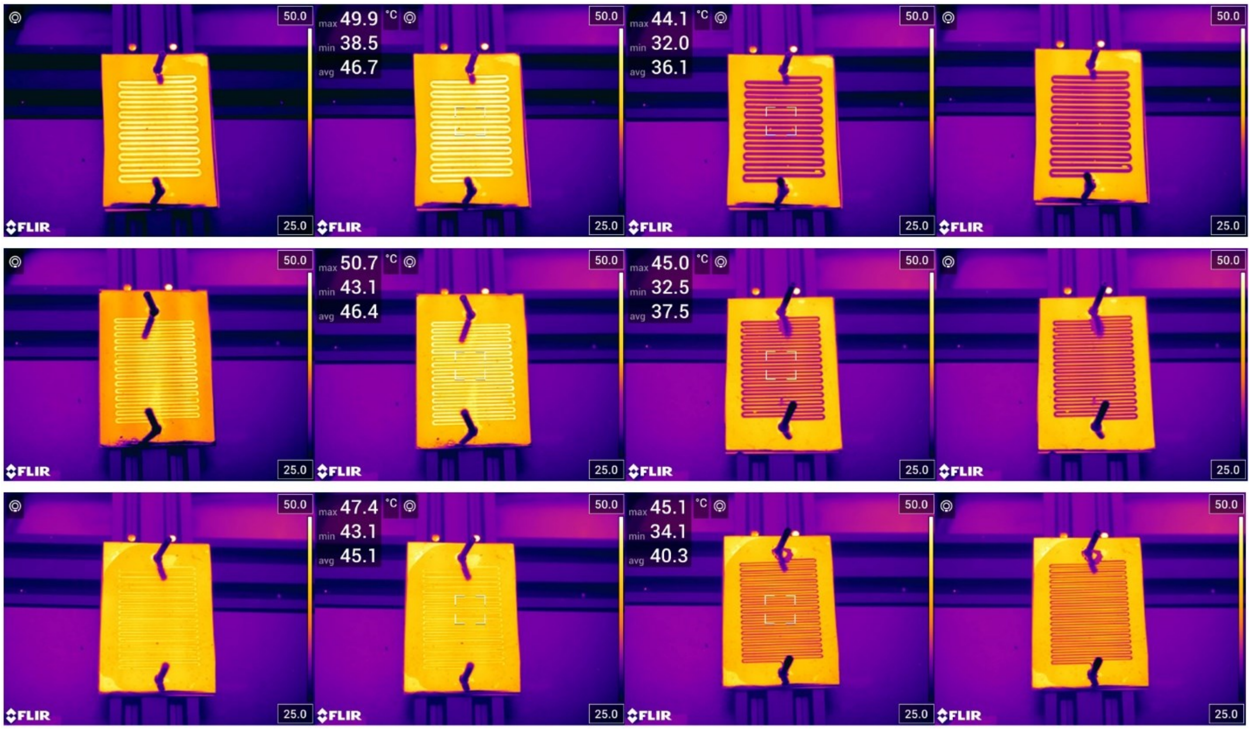

Figure A6. shows the raw images directly captured from the FLIR IR camera, the first row is the W3, the second row is W2, and the third row is W1 configuration. The first column is the unfilled channels, the second and third columns are the images with the measured data, and the fourth column is the filled channel IR appearance. The temperature bar is configured as 25-50°C to present better contrast.

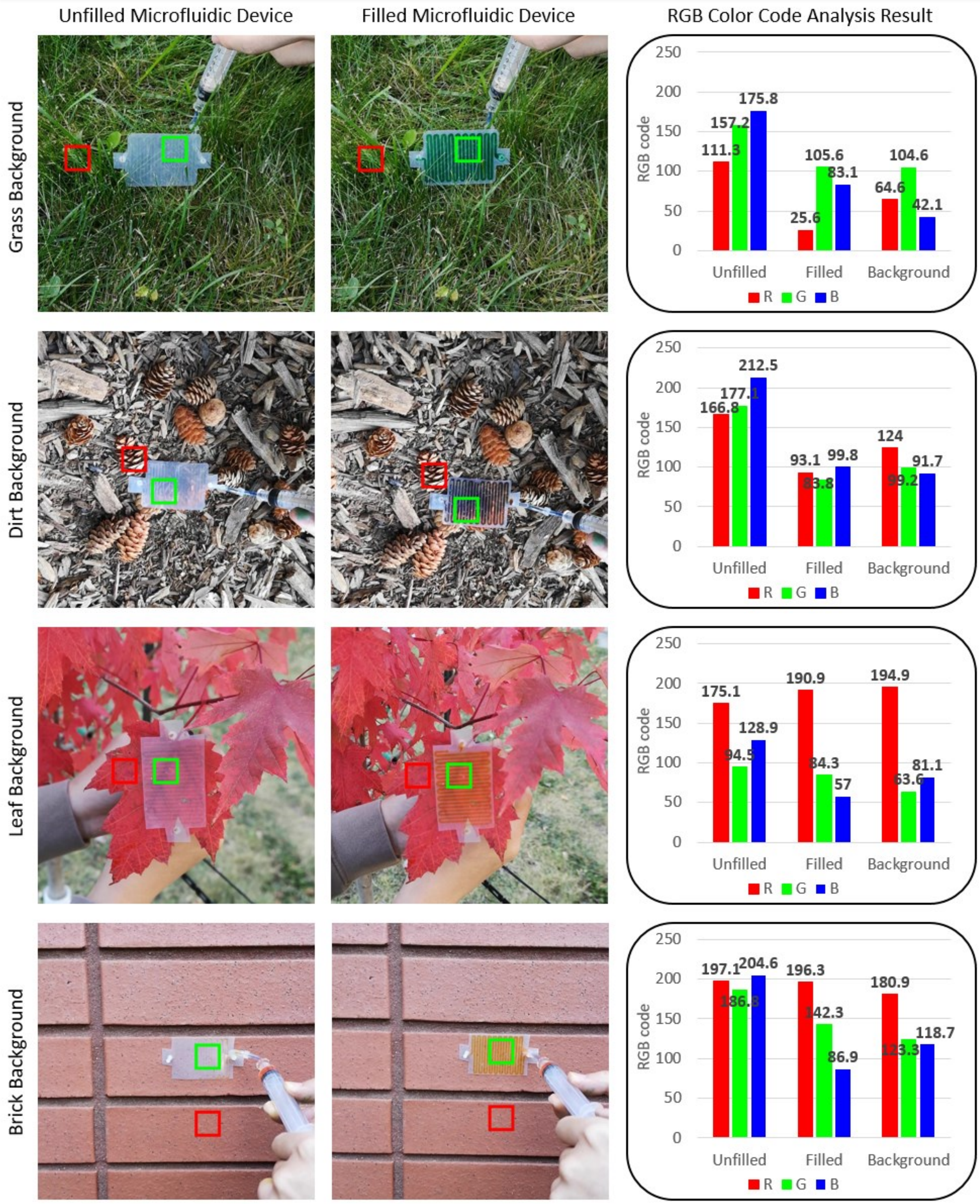

Figure A7. Shows the detailed RGB value in the third column.

Code for canny edge finding:

```
% Read an image and convert it to grayscale
img = imread('green0.png');
gray = rgb2gray(img);

% Apply a Gaussian filter to the image
gauss = imgaussfilt(gray, 3);

% Compute the gradient magnitude and direction using Sobel operators
[Gx, Gy] = imgradientxy(gauss);

% Compute the gradient magnitude and direction
gradient = sqrt(Gx.^2 + Gy.^2);
direction = atan2(Gy, Gx);

% Non-maximum suppression
suppressed = nlfilter(gradient, [3 3], @(x) max(x(:)));

% Double thresholding
high_threshold = 0.25 * max(suppressed(:));
low_threshold = 0.05 * high_threshold;
potential_edges = zeros(size(gradient));
potential_edges(suppressed > high_threshold) = 1;

% Edge tracking by hysteresis
final_edges = zeros(size(gradient));
while any(potential_edges(:))
    [r, c] = find(potential_edges, 1);
    final_edges(r, c) = 1;
    potential_edges(r, c) = 0;
    for rr = -1:1
        for cc = -1:1
            if r+rr > 0 && r+rr <= size(gradient, 1) && c+cc > 0 && c+cc <= size(gradient,
2) && final_edges(r+rr, c+cc) ~= 1 && suppressed(r+rr, c+cc) > low_threshold
                final_edges(r+rr, c+cc) = 1;
                potential_edges(r+rr, c+cc) = 0;
            end
        end
    end
end

% Show the edges
figure;
imshow(final_edges);
```

Code for color matching:

```
clc;
clear;
% Read in the image file
img = imread('red0.png');

% Define the size and location of the two regions
size_region = [100,100];
location1 = [580,330];
location2 = [580,510];

% Crop the regions from the image
region1               =               img(location1(1):location1(1)+size_region(1)-1,
location1(2):location1(2)+size_region(2)-1, :);
region2               =               img(location2(1):location2(1)+size_region(1)-1,
location2(2):location2(2)+size_region(2)-1, :);

% Calculate the mean color difference between the two regions
%diffR = mean((mean(region1(:,:,1)) - mean(region2(:,:,1)))*10/255);
%diffG = mean((mean(region1(:,:,2)) - mean(region2(:,:,2)))*10/255);
%diffB = mean((mean(region1(:,:,3)) - mean(region2(:,:,3)))*10/255);
%diff = (abs(diffR) + abs(diffG) + abs(diffB))/3;
% Plot the image
imshow(img);
hold on;

% Plot the first region
rectangle('Position',  [location1(2),  location1(1),  size_region(2),  size_region(1)],
'EdgeColor', 'r','LineWidth', 10);
%text(location1(2)+size_region(2)/2,   location1(1)+size_region(1)/2,   'Region   1',
'Color',
'white','HorizontalAlignment','center','VerticalAlignment','middle','fontsize',14,'fo
ntweight','bold');

% Plot the second region
rectangle('Position',  [location2(2),  location2(1),  size_region(2),  size_region(1)],
'EdgeColor', 'g','LineWidth', 10);
%text(location2(2)+size_region(2)/2,   location2(1)+size_region(1)/2,   'Region   2',
'Color',
'white','HorizontalAlignment','center','VerticalAlignment','middle','fontsize',14,'fo
ntweight','bold');

% Print the color difference value
region1R = mean((mean(region1(:,:,1))));
region1G = mean((mean(region1(:,:,2))));
region1B = mean((mean(region1(:,:,3))));
region2R = mean((mean(region2(:,:,1))));
region2G = mean((mean(region2(:,:,2))));
region2B = mean((mean(region2(:,:,3))));
disp(region1R);
disp(region1G);
disp(region1B);
disp(region2R);
disp(region2G);
disp(region2B);
```